

Phase Curves of Kuiper Belt Objects, Centaurs, and Jupiter Family Comets from the ATLAS Survey

MATTHEW M. DOBSON,¹ MEGAN E. SCHWAMB,¹ SUSAN D. BENECCHI,² ANNE J. VERBISCHER,³ ALAN FITZSIMMONS,¹
LUKE J. SHINGLES,^{4,1} LARRY DENNEAU,⁵ A. N. HEINZE,⁶ KEN W. SMITH,¹ JOHN L. TONRY,⁵ HENRY WEILAND,⁵ AND
DAVID. R. YOUNG¹

¹*Astrophysics Research Centre, School of Mathematics and Physics, Queen's University Belfast, Belfast BT7 1NN, UK*

²*Planetary Science Institute, 1700 East Fort Lowell Rd., Suite 106, Tucson, AZ 85719, USA*

³*Department of Astronomy, University of Virginia, P.O. Box 400325, Charlottesville, VA 22904-4325, USA*

⁴*GSI Helmholtzzentrum für Schwerionenforschung, Planckstraße 1, 64291 Darmstadt, Germany*

⁵*University of Hawaii Institute for Astronomy, 2680 Woodlawn Dr., Honolulu, HI 96822*

⁶*DiRAC Institute and the Department of Astronomy, University of Washington, 3910 15th Avenue NE, Seattle, WA 98195*

ABSTRACT

The Kuiper belt objects, the Centaurs, and the Jupiter-family comets form an evolutionary continuum of small outer Solar System objects, and their study allows us to gain insight into the history and evolution of the Solar System. Broadband photometry can be used to measure their phase curves, allowing a first-order probe into the surface properties of these objects, though limited telescope time makes measuring accurate phase curves difficult. We make use of serendipitous broadband photometry from the long-baseline, high-cadence ATLAS survey to measure the phase curves for a sample of 18 Kuiper belt objects, Centaurs, and Jupiter-family comets with unprecedentedly large datasets. We find phase curves with previously reported negative slopes become positive with increased data and are thus due to insufficient sampling of the phase curve profile, and not a real physical effect. We search for correlations between phase curve parameters, finding no strong correlations between any parameter pair, consistent with the findings of previous studies. We search for instances of cometary activity in our sample, finding a previously reported outburst by Echeclus and a new epoch of increased activity by Chiron. Applying the main belt asteroid HG_1G_2 phase curve model to three Jupiter-family comets in our sample with large phase angle spans, we find their slope parameters imply surfaces more consistent with those of carbonaceous main belt asteroids than silicaceous ones.

1. INTRODUCTION

Kuiper belt objects (KBOs) are small planetesimals residing beyond the orbit of Neptune and are the remnants of planet formation during the early history of the Solar System. Over 3700 KBOs¹ have been discovered to date, and can be divided into sub-populations based on their present dynamics (Delsanti & Jewitt 2006; Gladman et al. 2008; Kavelaars et al. 2008) and physical properties (Schaller & Brown 2007a; Brown 2008; Brown et al. 2011). Originating from the Kuiper belt population, the Centaurs are small icy objects that have diffused inwards onto giant planet-crossing orbits (Levison & Duncan 1997; Duncan & Levison 1997; Volk & Malhotra 2008). Centaurs are likely precursors to certain populations of short-period comets, most notably the Jupiter-family comets (JFCs) (Tiscareno & Malhotra 2003; Fernández et al. 2013; Bauer et al. 2013; Sarid et al. 2019), whose orbital dynamics are governed predominantly by Jupiter's gravitational influence (Vaghi 1973; Carusi & Valsecchi 1987; Levison & Duncan 1994; Levison 1996; Gladman et al. 2008; Sarid et al. 2019) and whose perihelion distances bring them sufficiently close to the Sun for water ice to sublimate (Womack et al. 2017 and references therein). Studying these populations of primordial objects can reveal information about the conditions, dynamics and evolutionary processes of the Solar System, both in its early history and its present state.

Broadband photometry remains the fastest method of characterizing large numbers of these objects, as they are generally too faint for spectroscopy. Such photometry can be used to analyse their phase curves: the change in an object's distance-corrected brightness when observed at different solar phase angles α , the angle between the Sun and

¹ From Minor Planet Center: <https://www.minorplanetcenter.net>

the observer as viewed from the object. The phase curve of an atmosphereless object is determined by its surface reflectivity, itself a complex function of its surface properties. Thus, analysis of an object's phase curve can allow an explorative probe into its overall surface properties (Hapke 1963, 1966, 1968, 1981, 1984, 1986, 2002, 2008, 2012, 2021; Bowell et al. 1989; Nelson et al. 2000; Belskaya et al. 2008; Verbiscer & Helfenstein 1998; Verbiscer et al. 2013).

The large heliocentric distances of KBOs and many Centaurs limit Earth-based observations of these objects to a narrow range of small phase angles ($\alpha \lesssim 2$ deg), requiring in-situ measurements from spacecraft for high phase angles. Verbiscer et al. (2019) and Verbiscer et al. (2022) obtained phase curves of KBOs spanning several dynamical sub-populations by combining data from both Earth-based observations and *NASA's New Horizons* spacecraft, extending the phase angle coverage beyond that achievable from Earth. The phase curves of the KBOs analysed were found to exhibit similarities to those of other populations of small Solar System bodies, including JFCs and giant planet satellites theorized to be captured KBOs (Verbiscer et al. 2019). Additionally, KBOs with high-albedo surfaces dominated by volatile ices were found to exhibit shallow phase curve slopes, with steeper slopes being a feature of objects with lower-albedo surfaces (Li et al. 2015; Ayala-Loera et al. 2018; Verbiscer et al. 2022). Without such measurements, the small phase angle range observable from Earth impairs the ability of surface reflectance models to accurately fit the data. However, beyond the very small range of phase angles where the opposition surge - the sudden increase in an object's brightness as $\alpha \rightarrow 0$ deg - is significant, Centaur and KBO phase curves typically exhibit approximately linear profiles across phase angles observable from Earth (Binzel & Mulholland 1984; Tholen & Tedesco 1994; Buie et al. 1997; Sheppard & Jewitt 2002; Schaefer & Rabinowitz 2002; Rabinowitz et al. 2006, 2007; Sheppard 2007; Belskaya et al. 2008; Schaefer et al. 2009; Verbiscer et al. 2013), with a slope quantified by the linear phase coefficient, β . Fitting a linear function to the phase curves generated using Earth-based observations has thus allowed comparison of phase curves between individual objects and populations.

Rabinowitz et al. (2007) and Schaefer et al. (2009) found phase curves of KBOs and Centaurs to exhibit approximately linear trends when observed from Earth. These phase curves ranged from flat to steep in profile, with varying phase coefficient values between different photometric filters. The largest KBOs exhibited small phase coefficients ($\beta < 0.1$ mag deg⁻¹), suggesting such a property may be indicative of objects with high-albedo volatile-rich surfaces, in accordance with both the findings of Verbiscer et al. (2022) and theoretical models of surface reflectivity. Several Centaurs also exhibited similarly flat phase curves, implying their surfaces are dominated by organic compounds. This accords with the findings of Sheppard & Jewitt (2002), laboratory measurements of both high- and low-albedo materials (Shkuratov et al. 2002) and the improbability of volatile retention by Centaurs due to their smaller heliocentric distances. Schaefer et al. (2009) reported correlations between an object's opposition surge with its color index and geometric albedo. Both Schaefer et al. (2009) and Verbiscer et al. (2019) find a distinction between the scattering properties of outer Solar System satellites and those of the Centaur and KBO populations. The studies of Alvarez-Candal et al. (2016); Ayala-Loera et al. (2018); Alvarez-Candal et al. (2019) report several phase coefficients for Centaurs and KBOs whose values were significantly negative, implying unphysical dimming at small phase angles which cannot be explained by surface reflectivity models. These studies also reported a strong correlation between the relative phase coefficient between filters (defined by Alvarez-Candal et al. (2019) as $\Delta\beta \equiv \beta_V - \beta_R$) and an object's color index ($H_V - H_R$), in addition to a correlation between relative phase coefficient and albedo for objects with absolute magnitudes $H_V \geq 4.5$. Kokotanekova et al. (2017) and Kokotanekova et al. (2018) measured shallow phase coefficients of $\beta < 0.1$ mag deg⁻¹ for 14 JFCs, and reported a possible correlation of increasing geometric albedo with steeper phase coefficient.

Phase curve measurements require high-cadence observations over a long baseline to sample the full range of phase angles visible from Earth. Such ideal measurements are difficult to achieve in practice, due to the limited availability of telescope time, in addition to the challenges of ground-based observations. Combining data of an object from multiple telescopes at different sites, as well as from literature studies, can help augment otherwise sparse datasets (Alvarez-Candal et al. 2016; Ayala-Loera et al. 2018; Alvarez-Candal et al. 2019). However, this could introduce systematic errors into the dataset due to heterogeneous data reduction pipelines and differing broadband filter wavelength ranges, as well as potential long timespans between observations. To sample the full range while ensuring all data come from a homogeneous photometric system and data reduction pipeline would require observations with a telescope that performs regular-cadence observations of that object. Such an opportunity is afforded by the Asteroid Terrestrial-impact Last Alert System (ATLAS) survey (Tonry et al. 2018a,b), which has accumulated large datasets of serendipitous observations of many KBOs, Centaurs, and JFCs.

In this paper, we make use of the high-cadence, long baseline photometry obtained by the ATLAS survey to generate phase curves for a sample of KBOs, Centaurs, and JFCs visible to the ATLAS telescopes in two broadband filters. With the advantage of a larger dataset than previous studies across a single baseline, we measure the phase coefficients of these objects, search for correlations between these and other object parameters, and look for outbursts of cometary activity across the survey’s near-continuous, 6-year observation baseline. This paper is structured as follows. In section 2, we describe the ATLAS survey. Section 3 details the sample of objects selected for this study. In section 4, we present details about the photometry obtained by and used in this study. Section 5 details the data analysis methods, while the results from this analysis and our discussion of these are presented in Sections 6. Finally, in Section 7, we draw our conclusions from our analysis.

2. ATLAS

The data used in this study originate from observations performed by the ATLAS wide-field survey (Tonry et al. 2018a), whose primary mission is to detect near-Earth asteroids that may pose an impact hazard to Earth. Since its first observations in 2016, ATLAS has serendipitously observed a sample of bright KBOs, Centaurs, and JFCs, with the long baseline and high cadence of observations providing ample sampling of the phase curves of these objects. This eliminates the need to include additional data from external sources, thereby reducing systematic errors that could arise from combining data obtained via heterogeneous methods of image processing and data analysis. ATLAS’s long baseline has been previously utilized by studies analysing other populations of small Solar System objects, such as asteroids (Erasmus et al. 2020; Mahlke et al. 2021) and Jupiter Trojans (McNeill et al. 2021).

ATLAS presently consists of four 0.5-m Schmidt telescopes, two of which are located at Hawai’i (sites at Haleakalā and Maunaloa), with another two installed in 2022 at sites in Chile and South Africa. The ATLAS telescopes regularly observe the sky outside 60 deg of the Sun to a limiting magnitude of approximately 19.5 mag in two non-standard wide-band filters - *cyan* (*c*, spanning 420-650 nm) and *orange* (*o*, spanning 560-820 nm). When weather conditions permit, four 30s exposures are taken per pointing over a 1 hour interval. Each exposure covers 28.9 deg² field of view (Tonry et al. 2018a,b), with the two telescopes of ATLAS installed at the time of this study covering the entire accessible sky over approximately 2 days. Further details of the ATLAS system and data reduction pipeline are described in Tonry et al. (2018a,b) and Smith et al. (2020). For this study, we make use of data from the two ATLAS telescopes at the Hawai’ian sites of Haleakalā and Maunaloa, as the southern hemisphere telescopes had only recently been installed at the time of this study.

3. SAMPLE OF OBJECTS

We select objects from the KBO, Centaur and JFC populations that may have been observable by ATLAS, downloading the 2021 catalog of objects from JPL Horizons². These objects are selected according to the following criteria:

1. The semimajor axis of each object must lie beyond the aphelion of Jupiter ($a > 5.5$ au).
2. For ≥ 1 month during the ATLAS baseline, the object must be brighter than 19.5 mag (ATLAS limiting magnitude) to ensure detection.
3. The objects’ predicted positional uncertainties had to be $< 1''$ (equating to ~ 0.5 pixels on ATLAS images), to ensure proper identification on the ATLAS images;
4. The ATLAS observations of each object had to span $> 50\%$ of the total observable phase angle range during the time that ATLAS has been observing, to ensure adequate sampling of at least half the observable span of the phase curve;
5. Each object had to have at least 50 observations recorded in both *c* and *o* filters, to ensure adequate sampling.

Upon selecting our sample of objects, we subsequently divide them into their dynamical classes. We define KBOs as small outer Solar System objects whose semimajor axes lie beyond that of Neptune ($a > a_N$). The KBOs in our sample come from several dynamically hot sub-populations of the Kuiper belt using the definitions of Gladman et al. (2008): 3 objects from the resonant population (Pluto, Orcus, Huya), 1 from the detached TNO population (Eris),

² <https://ssd.jpl.nasa.gov/> - retrieved on 2021 March 25

Table 1. Classification of objects used in this study with semimajor axes $5.5 \text{ au} < a < 30.1 \text{ au}$, according to the definitions of Gladman et al. (2008), Jewitt (2009) and Sarid et al. (2019).

Name	Gladman et al. (2008)	Jewitt (2009)	Sarid et al. (2019)	This study
(944) Hidalgo	JFC	JFC	Neither	JFC
(2060) 95P/Chiron	Centaur	Centaur	Centaur	Centaur
(10199) Chariklo	Centaur	Centaur	Centaur	Centaur
(37117) Narcissus	JFC	JFC	Neither	JFC
(54598) Bienor	Centaur	Centaur	Centaur	Centaur
(60558) 174P/Echeclus	JFC	Centaur	Centaur	Transition Object
(347449) 2012 TW236	JFC	JFC	Neither	JFC
(349933) 2009 YF7	JFC	Centaur	Centaur	Transition Object
(459865) 2013 XZ8	Centaur	Centaur	Centaur	Centaur
(501585) 2014 QA43	JFC	JFC	Neither	JFC
2016 ND21	JFC	JFC	Neither	JFC

and 3 from the hot classical Kuiper belt (Haumea, Quaoar, Makemake). Furthermore, 6 of our 7 KBOs, with absolute magnitudes $H_V < 3$, differ significantly from the remainder of the Kuiper belt. These Pluto-sized objects have greater masses, allowing retention of high albedo volatiles on their surfaces, augmenting their absolute magnitude such that they deviate from the brightness distribution of the Kuiper belt (Bernstein et al. 2004; Schaller & Brown 2007b; Brown 2008, 2012).

At present, there is no agreed upon definition for the Centaur population, nor is there a consensus distinction between the Centaurs and the related JFC population (Levison & Duncan 1997; Gladman et al. 2008; Jewitt 2009; Kokotanekova et al. 2017; Chandler et al. 2020; Lilly et al. 2021; Roberts & Muñoz-Gutiérrez 2021). For our study, we use a dynamical definition to separate these populations not based on past histories of cometary activity. We define and distinguish between the Centaur and JFC populations by their semimajor axes, perihelia, and the effect of Jupiter on their dynamics, the latter of which can be quantified by the Tisserand parameter with respect to Jupiter, T_J , defined as:

$$T_J \equiv \frac{a_J}{a} + 2 \cos i \sqrt{\frac{a}{a_J} (1 - e^2)} \quad (1)$$

where a and a_J are the semimajor axes of the object and Jupiter respectively, e the object’s eccentricity and i the object’s inclination. We construct our Centaur definition based on those of Gladman et al. (2008) and Jewitt (2009), classifying Centaurs as small Solar System objects not in 1:1 mean motion resonance with any planet, on orbits with semimajor axes a and perihelia q between the semimajor axes of Jupiter and Neptune ($a_J < a, q < a_N$), and Tisserand parameters with respect to Jupiter $T_J > 3.05$, this threshold value accounting for Jupiter’s non-zero eccentricity and the resulting effect on small object dynamics (Gladman et al. 2008). We accordingly define Jupiter-family comets (JFCs) as small Solar System objects not in 1:1 mean motion resonance with a planet, whose perihelia lie interior to the orbit of Jupiter ($q < a_J$) and with Tisserand parameters with respect to Jupiter of $2 < T_J \leq 3.05$. We classify any objects in our sample with $a < a_N$ that do not satisfy the definitions for Centaurs or JFCs as *Transition Objects*. Table 1 lists the objects in our sample with semimajor axes $a < a_N$, and their dynamical classification according to the definitions of Centaurs and JFCs from Gladman et al. (2008), Jewitt (2009) and Sarid et al. (2019), in addition to their classification in this study.

Our sample consists of 18 objects (7 KBOs, 4 Centaurs, 5 JFCs, and 2 Transition Objects), whose orbital parameters are listed in Table 2, along with their estimated V-band absolute magnitudes, and, if known, their published rotational lightcurve periods and amplitudes. The orbital distribution of our sample is shown in Figure 1 and its H distribution is plotted in Figure 2. There are a median of 181 and 463 ATLAS observations per object in the c and o filters,

Table 2. Heliocentric orbital elements, absolute magnitudes and rotation periods of KBOs, Centaurs, JFCs and Transition Objects visible to ATLAS survey used in this study. a = semimajor axis; e = eccentricity; i = inclination; q = perihelion; Q = aphelion; T_J = Tisserand parameter (with respect to Jupiter); H = (V -band) absolute magnitude; P = rotation period; ΔM = peak-to-peak rotational lightcurve amplitude.

Name	a	e	i	q	Q	T_J	H	P	ΔM	Source for P	Dynamical Class
	(au)		(deg)	(au)	(au)		(mag)	(hrs)	(mag)	and ΔM	
(136199) Eris	67.94	0.43	43.97	38.41	97.51	4.780	-1.11	KBO (detached)
(136108) Haumea	43.12	0.2	28.21	34.65	51.54	5.086	0.25	3.915341	0.28	SS17	KBO (hot classical)
(38628) Huya	39.69	0.28	15.47	28.55	50.49	5.235	4.86	5.28	0.02 \pm 0.01	T14	KBO (3:2 resonant)
								4.45	0.1	G16	
								6.75	< 0.1	O03	
(136472) Makemake	45.37	0.16	28.99	37.98	52.77	5.204	-0.13	22.83	0.032 \pm 0.005	H19	KBO (hot classical)
									0.0286 \pm 0.0016	HL09	
(90482) Orcus	39.14	0.23	20.59	30.21	48.06	5.129	2.3	10.5	\sim 0.05	G16	KBO (3:2 resonant)
									0.18 \pm 0.08	R06	
									0.03-0.18	D10	
									0.06 \pm 0.04	O11	
(134340) Pluto	39.45	0.25	17.09	29.57	49.32	5.228	-0.4	153.29352	0.19	B18	KBO (3:2 resonant)
									(Pluto+Charon)		
(50000) Quaoar	43.66	0.04	7.99	41.85	45.35	5.844	2.51	8.8394	0.17 \pm 0.04	O03	KBO (hot classical)
									0.17	FB10	
(459865) 2013 XZ8	13.42	0.37	22.53	8.42	18.41	3.140	9.69	Centaur
(54598) Bienor	16.46	0.2	20.75	13.18	19.71	3.578	7.55	9.14	0.7	O02	Centaur
									0.75 \pm 0.09	O03	
									0.34 \pm 0.08	R06	
									0.088 \pm 0.008 (2014)	FV17	
									0.082 \pm 0.007 (2015)	FV17	
									0.10 \pm 0.02 (2016)	FV17	
(10199) Chariklo	15.84	0.17	23.35	13.17	18.52	3.485	6.54	7.004	0.11-0.13	F14	Centaur
									0.06 \pm 0.02	L17	
95P/(2060) Chiron	13.69	0.38	6.93	8.52	18.87	3.365	5.84	5.918	0.088 \pm 0.003	LJ90	Centaur
									0.07 \pm 0.02	D91	
									0.04 \pm 0.005	MB93	
									0.06 \pm 0.01	L97	
(347449) 2012 TW236	6.97	0.57	11.96	3.0	10.94	2.610	12.3	JFC
(501585) 2014 QA43	9.66	0.51	37.21	4.76	14.54	2.409	11.4	11.558	0.236	S18	JFC
2016 ND21	8.47	0.56	21.83	3.76	13.16	2.584	12.3	17.53	0.31	H19	JFC
(944) Hidalgo	5.73	0.66	42.54	1.95	9.52	2.068	10.69	10.0630	0.48	W97	JFC
(37117) Narcissus	6.88	0.55	13.8	3.07	10.68	2.616	13.29	JFC
(349933) 2009 YF7	12.11	0.46	30.99	6.51	17.72	2.749	10.91	Transition Object
174P/(60558) Echeclus	10.71	0.46	4.34	5.81	15.60	3.031	9.17	26.802	0.24 \pm 0.06 (R-filter)	R05	Transition Object
									0.36 \pm 0.09 (V-filter)	R05	

References—Heliocentric orbital elements and absolute magnitude values obtained from JPL Horizons. Rotational period/amplitude sources: B18: Benecchi et al. (2018), SS17: Santos-Sanz et al. (2017), O03: Ortiz et al. (2003), FB10: Fraser & Brown (2010), LJ90: Luu & Jewitt (1990), D91: Dahlgren et al. (1991), MB93: Marcialis & Buratti (1993), L97: Lazzaro et al. (1997a), FV17: Fernández-Valenzuela et al. (2017), O02: Ortiz et al. (2002), D10: Delsanti et al. (2010), O11: Ortiz et al. (2011), G16: Galiazzo et al. (2016), F14: Fornasier et al. (2014), L17: Leiva et al. (2017), R05: Rousselot et al. (2015), HL09: Heinze & de Lahunta (2009), H19: Hromakina et al. (2019), T14: Thirouin et al. (2014), S18: Safrit (2018), W97: Wisniewski et al. (1997).

respectively. Across all objects in this study, the ATLAS data cover a median of 93% (c) and 95% (o) of the total observable phase angle range from Earth across the ATLAS baseline. These objects span apparent magnitudes $14.2 < c < 19.8$ and $13.8 < o < 19.7$ in each ATLAS photometric filter. The galactic latitudes spanned by our sample of objects during the ATLAS baseline are shown in Figure 3, showing many objects in our sample cross into the galactic plane where stellar crowding and the resulting background flux contamination must be dealt with.

4. DATA AND PHOTOMETRY

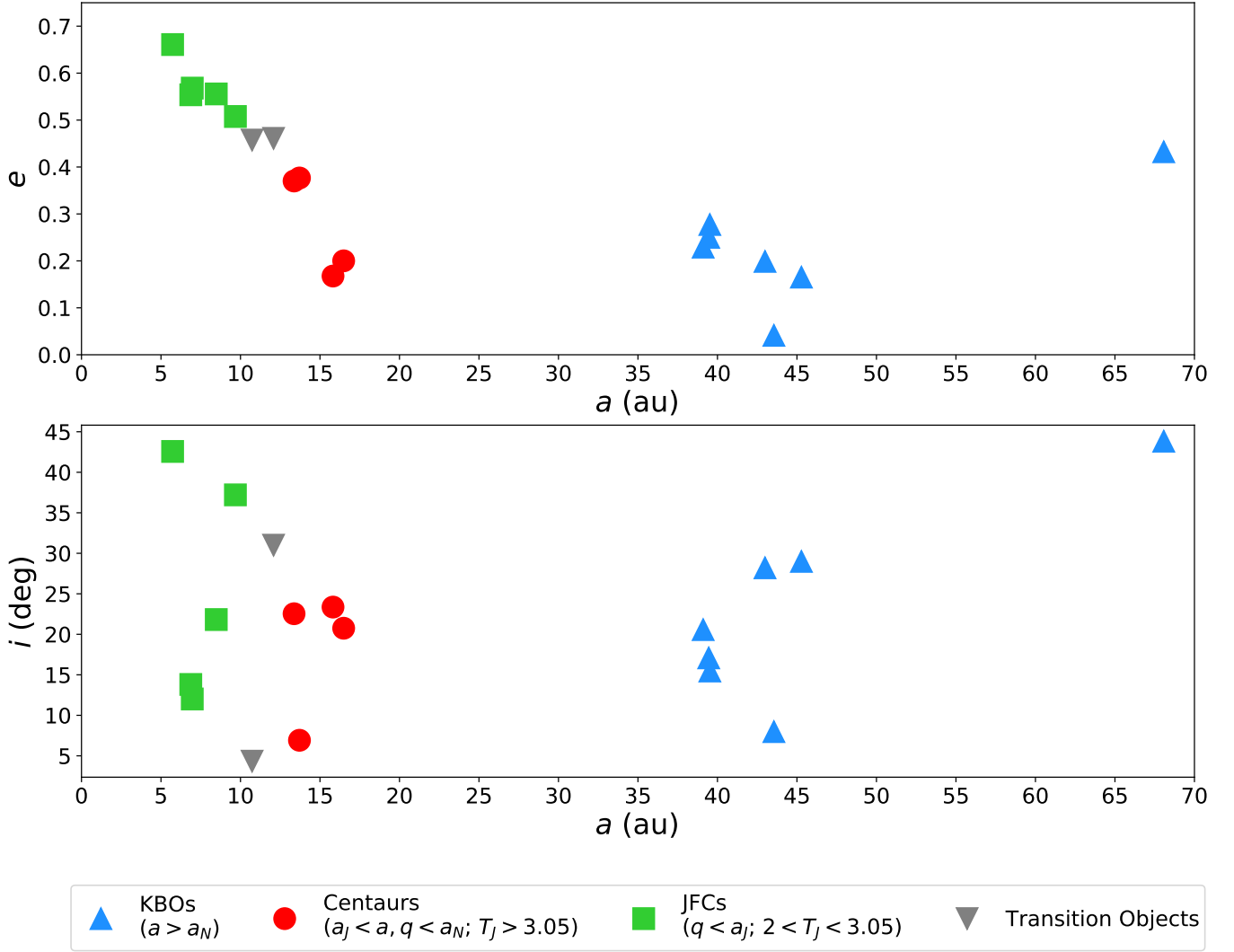


Figure 1. Orbital distribution diagram showing semimajor axes (a), orbital eccentricities (e) and orbital inclinations (i) of the objects used in this study. Data taken from JPL Horizons.

We utilize observations made by the two ATLAS telescopes at Haleakalā and Maunaloa. Data for our sample was obtained using the ATLAS Forced Photometry Server³ (Shingles et al. 2021), which fits a point-spread function (PSF) at an object’s position on the image of an observation as predicted from its orbital ephemeris cataloged by the Minor Planet Center, calculating the AB magnitude of the flux at that point. The ATLAS data reduction includes an image subtraction pipeline, which matches a high signal-to-noise reference image of the static sky (“wallpaper”) to the location of a given observation’s image, and subtracts the wallpaper flux from that image, creating a “difference image” containing only the flux not previously present (Tonry et al. 2018a,b). We chose to use difference images to reduce the effect of contaminating background stars and galaxies on the brightness measurements of each object, which can become significant if an object passes in front of or near a background star on the sky. We select all ATLAS data up to and including the most recent observations at the time of selection (2021 June 30), allowing us to obtain sufficient photometry to generate phase curves for all 18 objects in our sample in both c and o filters. We deem any observation a detection if its apparent magnitude is brighter than 1) the 5σ limiting magnitude of the image (to ensure the observation was of good quality); and 2) the 3σ upper magnitude limit derived from the flux uncertainty (ensuring an observed object could be detected on the image). For every detection that satisfies these criteria, we correct their

³ <https://fallingstar-data.com/forcedphot/>

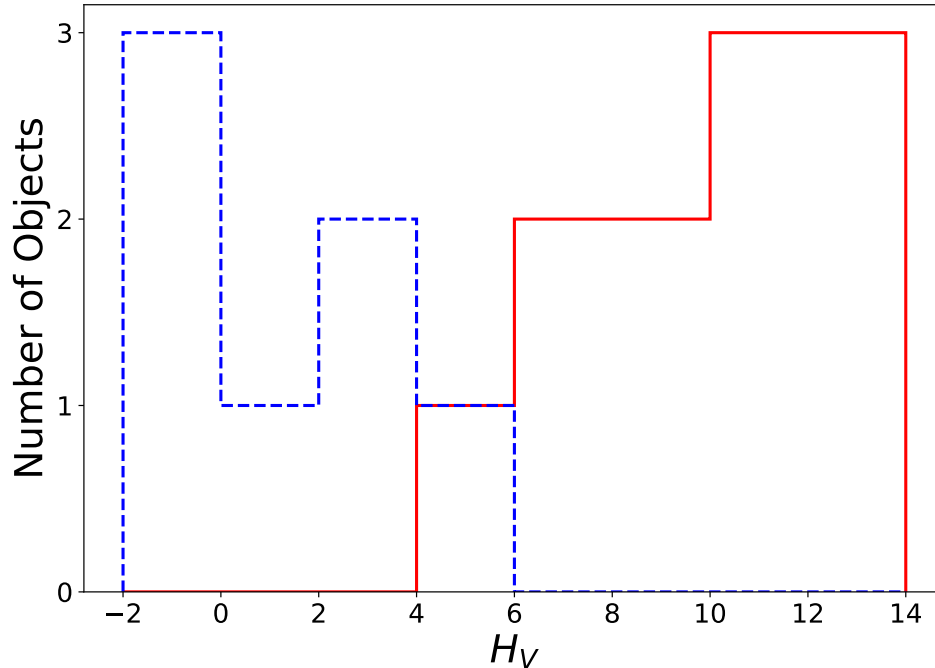


Figure 2. Histogram of V -band absolute magnitudes from JPL Horizons of the sample of objects with semimajor axis less than Neptune’s $a < a_N$ (solid red) and greater than Neptune’s $a > a_N$ (dashed blue) used in this study. Bin-size = 2 mag.

Table 3. ATLAS photometry for each object.

Name	MJD (light travel time-corrected)	Phase (deg)	Apparent Magnitude	Apparent Magnitude Uncertainty	Filter	Reduced Magnitude	Flags
10199 Chariklo	57511.477108	3.1056	18.516	0.17	c	6.745	G
10199 Chariklo	57891.519318	2.689	18.771	0.151	o	6.935	G
10199 Chariklo	57895.513409	2.5112	18.579	0.115	c	6.749	G
10199 Chariklo	57903.490523	2.1231	19.009	0.124	c	7.189	G
10199 Chariklo	57903.507429	2.1222	19.243	0.129	c	7.423	G

NOTE—This table is published in its entirety in the machine-readable format. A portion is shown here for guidance regarding its form and content.

NOTE—Key for flags: G - data used to measure phase curve parameters; C - cometary activity flagged by detection algorithm; D - data not flagged by algorithm yet obtained during extended cometary activity; O - opposition effect.

Modified Julian Dates (MJDs) for light travel time. The ATLAS photometry used in this analysis for all objects in our sample are listed in Table 3.

5. DATA ANALYSIS

We detail the methods used to fit the phase curves for our sample in both ATLAS c and o filters, search for rotational lightcurves in the ATLAS data, detect for epochs of cometary activity, and re-fit the data corrected for these effects.

5.1. Generating Phase Curves

All ATLAS apparent magnitude measurements were transformed to reduced magnitudes to remove distance effects. The reduced magnitude M is defined as:

$$M = m - 5 \log_{10}(r\Delta) \quad (2)$$

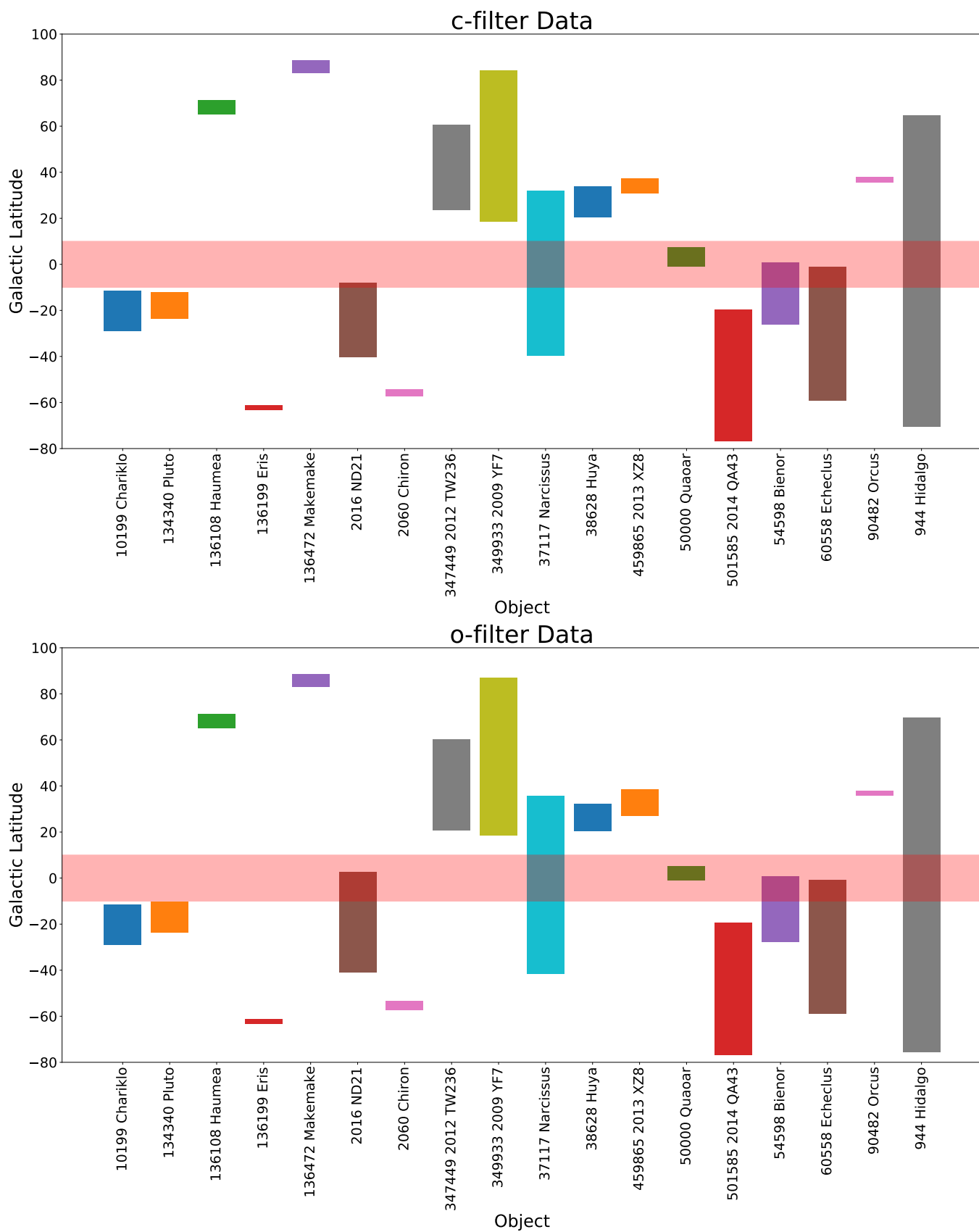


Figure 3. Bar plot of galactic latitude of observations for each object in ATLAS *c* (upper plot) and *o* (lower plot). The red bar denotes the sky region spanning ± 10 deg from the galactic equator.

where m is the apparent magnitude, and r and Δ are the heliocentric and geocentric distances of the object at the time of each observation, respectively. Distances and solar phase angles for each observation of a given object were obtained from JPL Horizons. The uncertainty in reduced magnitude was taken to be that of the measured apparent magnitude, due to the comparatively negligible uncertainties of the geocentric and heliocentric distances. Datapoints with uncertainties larger than 85% of all datapoints were removed. These observations were likely taken during poor observing conditions, causing their large uncertainties. Each object’s dataset was then clipped to remove outlying points beyond 3-sigma from the median reduced magnitude to exclude measurements from contaminating flux, poor image subtraction, or poor calibration. All data in a given filter were treated as a single bin of phase angle unless observations extended to phase angles >20 deg or <0.1 deg, where phase curve profiles become non-linear, in which cases data were split into two or four bins of phase angle, respectively. All data in each bin were sigma-clipped separately until convergence.

5.2. Phase Curve Fitting

Beyond very small phase angles ($\alpha \sim 0.1$ deg, Belskaya et al. 2008) where the opposition effect is significant, KBO, Centaur, and JFC phase curves exhibit approximately linear profiles when observed from Earth. We apply a weighted linear fit to the phase curve of each object in each ATLAS filter, using the *polyfit* function from the *NumPy* Python package (van der Walt et al. 2011; Harris et al. 2020) to fit a 1st-degree polynomial to the reduced magnitudes $M(\alpha)$ according to

$$M(\alpha) = H + \alpha\beta \quad (3)$$

where α is the solar phase angle of the object at the time of measurement, β is the linear phase coefficient, and H is the absolute magnitude of the object. We consider only data at phase angles $\alpha \geq 0.1$ deg to remove any influence of an opposition surge on the resulting β value. Each data point was weighted by the inverse of its magnitude uncertainty. The best fit values of both β and H and their associated uncertainties were computed via Monte Carlo simulation. We generate 10^5 synthetic phase curves with synthetic reduced magnitude measurements $M_{i,synthetic}$ calculated according to:

$$M_{i,synthetic} = M_i + rand[0, \delta M_i] \quad (4)$$

where $rand[0, \delta M_i]$ is a random number generated from a normal distribution centred at zero of standard deviation equal to δM_i , the uncertainty of each reduced magnitude measurement. The best fit β and H values were taken to be the medians of the distributions of all 10^5 results for each parameter. These distributions tended to be approximately Gaussian in profile, thus we took the associated uncertainties of these parameters to be half of the range that includes the central 95% of their corresponding distributions, yielding 2σ uncertainty values. Figure 4 shows an example for the KBO Quaoar of an ATLAS phase curve of our sample and the associated uncertainty distributions. For objects for which changes in brightness due to their periodic lightcurve or outbursts of cometary activity can be identified (applicable to 5 objects in total), we correct their datasets for these effects (see Sections 5.3 and 5.4 for lightcurve and cometary activity correction, respectively) and reapply the phase curve fitting algorithm to the corrected data.

5.3. Lightcurve Corrections

We aim to correct for the effect of rotational modulation on the phase curves wherever possible by searching for periodicities corresponding to the period of the rotational lightcurve of an object for all ATLAS data in our sample. For most objects in our sample, the uncertainty in the reduced magnitude measurements exceeds the literature peak-to-peak amplitude of the rotational lightcurve. This obscures any rotational modulation, thus precluding any correction of this effect on the phase curve of the object. However, for some objects in our sample we observe substructure in the residuals to the best-fitting linear phase curve function, which extends beyond the associated uncertainties of the brightness measurements, potentially due to rotational modulation.

To search for periodicities in the lightcurve, we use the Lomb-Scargle periodogram algorithm (Lomb 1976; Scargle 1982) due to the irregular time spacing of the ATLAS observations. For each filter, the best fit linear phase curve is subtracted from each dataset. The resulting data, corrected also for light travel time, were then passed into the Lomb Scargle periodogram function (*LombScargle*) from the *astropy Python* package (Astropy Collaboration et al. 2013, 2018), weighted by the reduced magnitude uncertainty. Frequency grids were chosen with minimum and maximum rotation frequencies of 0.1 day^{-1} (240 hr period) and 24 day^{-1} (1 hr period), with 10^7 periodogram evaluations between these frequency extremes. Potential rotation periods for each object in the sample were searched for in the c and o

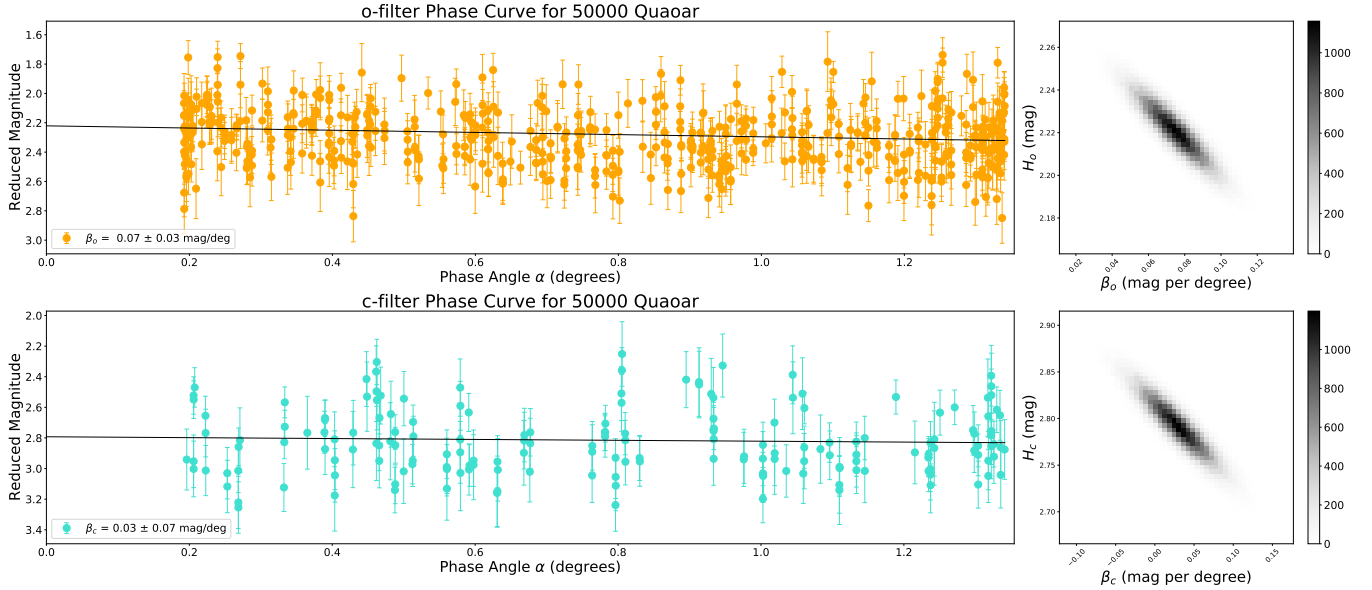


Figure 4. Linear fit to phase curve of (50000) Quaoar in c and o filters, with 2D histograms showing density plot of error distributions of linear phase coefficient and absolute magnitude. Best fit function extended to $\alpha = 0$ deg for ease of viewing the extrapolated absolute magnitude value and any potential opposition surge. The complete figure set (18 images) is available in the online published version of the paper.

datasets separately. For a given filter, the maximum peak in the power spectrum was taken to be the object’s best fitting period value, with its associated uncertainty equal to half the difference between the period values corresponding to the closest two stationary points either side the maximum peak.

We highlight that the best-fit period value is subject to uncertainty due to aliasing, background noise and uncertainties in the measured magnitudes (VanderPlas 2018). A method of quantifying the validity of a given rotation period is to calculate the false alarm probability of the maximum peak of the power spectrum - the probability that Gaussian noise could produce a signal of equal height to a given peak in the power spectrum (VanderPlas 2018). For the rotation period value yielded for each filter, we calculated false alarm probabilities, choosing the Baluev method (Baluev 2008) for its suitable accuracy and computational efficiency (VanderPlas 2018). Only objects whose periods in both filters came from peaks higher than the 95% false alarm probability level ($>2\sigma$ results) were considered to be plausible.

Large photometric uncertainties in the data, plus the generally fewer c filter observations compared to the o -filter, could mean that significantly different best-fit period values are yielded per filter. We set a criterion that the period values from both filters must match to <0.5 hours to be considered valid. For any object which fits this criterion, we check if their rotation periods match values aliased to Earth’s sidereal period (12, 24, 48, etc. hours) to <0.1 hours, to ensure we are not detecting periodicity due to sampling rate. If so, we check the rotation phase coverage of the data when phase-folded to the rotation period in each filter. If the phase-folded data of an object are grouped into clusters with gaps in between, or cover $<50\%$ of the rotation phase span, we reject that object’s rotation period value.

Three objects in our sample satisfy the above criteria for valid rotation periods: Pluto, Haumea, and Hidalgo. For these objects, we hence consider only the rotation period yielded by the filter with more datapoints (o). The ATLAS rotation period for Pluto is consistent with values from literature (Tholen & Tedesco 1994; Tholen & Buie 1997; Sheppard & Jewitt 2002; Schaefer et al. 2008; Buie et al. 2010; Benecchi et al. 2018) and, to within uncertainties, the ATLAS rotation periods equal the half-values of the literature rotation periods of Haumea (Rabinowitz et al. 2006; Lacerda et al. 2008; Lellouch et al. 2010; Thirouin et al. 2010; Lockwood et al. 2014) and Hidalgo (Hanus̄ et al. 2016; Santos-Sanz et al. 2017). We note that uncertainties in our reduced magnitude measurements could obscure double-peaked lightcurves of elongated or irregular-shaped objects, causing them to appear as single-peaked and the rotation period value yielded by the Lomb-Scargle algorithm to equate to half the true rotation period. Both Haumea (Rabinowitz et al. 2006; Lacerda et al. 2008; Lellouch et al. 2010; Thirouin et al. 2010; Lockwood et al. 2014) and Hidalgo (Durech et al. 2007; Hanus̄ et al. 2016) exhibit shape elongation. Our measured period values for these objects

LSP for 347449 2012 TW236

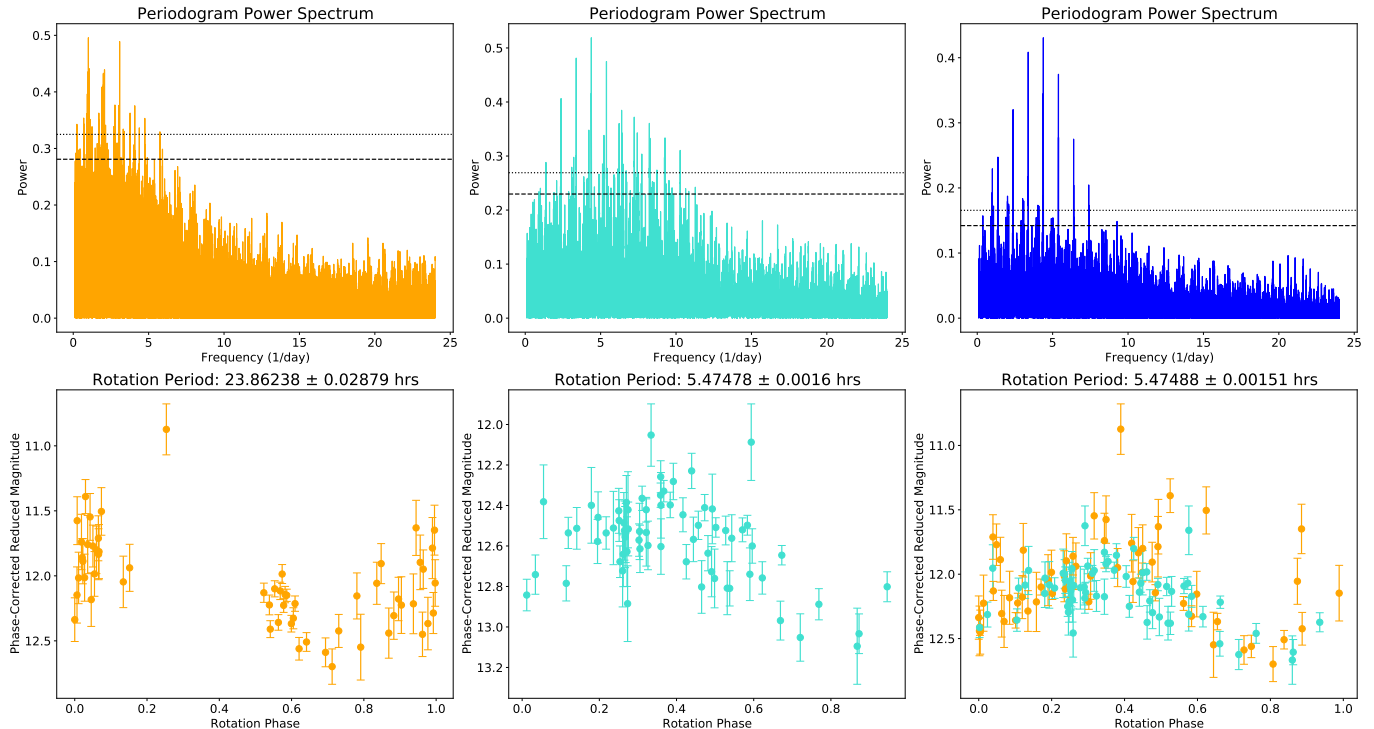


Figure 5. *Upper row:* Lomb-Scargle periodogram power spectra for 2012 TW236 in the *o* (orange), *c* (cyan), and combined *c* and *o* (blue) filters. The black dashed and dotted lines represent the 95% and 99.7% false alarm probability levels. *Lower row:* The *o* (orange, left), *c* (cyan, centre), and combined *c* and *o* (right) datasets of 2012 TW236, each phase-folded to the rotation period value corresponding to maximum peak in the power spectrum. The combined filter dataset shows a clear sinusoidal lightcurve.

are consistent with the half the reported rotation periods, thus we consider the true rotation period of these two objects to be twice the value output from the Lomb-Scargle Periodogram. The ATLAS rotation period values for Pluto, Haumea and Hidalgo, both those yielded by the maximum periodogram peak and the final chosen rotation period values, are listed in Table 5, in addition to those from literature.

Some rotation periods may not appear in individual filter datasets, but may be discerned when the datasets are combined to augment sampling of any rotational lightcurve. We repeat our Lomb-Scargle periodogram algorithm on both the ATLAS *c* and *o* filter data combined. We assume that the objects in our sample exhibit no variability in colour over their rotation periods, and correct the dataset in each filter for color according to the difference in the median reduced magnitudes of each filter per object. We consider only Lomb-Scargle periodogram spectra maxima higher than the 95% false alarm probability level. For objects which satisfy this criterion, we consider only those where the data in both filters span the full rotation phase space (ensuring that the rotation period value is not being driven by one filter only) and where the standard deviation of the datapoints exceeds twice the median magnitude uncertainty. If the object's phase-folded lightcurve exhibits gaps in the phase-folded lightcurve, and/or the rotation period value lies close to those aliased to Earth's sidereal period (12, 24, 48 etc. hours) to <0.1 hours, we reject the object's rotation period value. We recover rotation periods for Pluto, Haumea, and Hidalgo, all consistent to those found by separate analysis of each filter. We discover a rotation period value of 5.4749 ± 0.0015 hours from the Lomb-Scargle periodogram for the JFC 2012 TW236. The Lomb-Scargle periodogram power spectra and the datasets of 2012 TW236 phase-folded to the obtained rotation periods are shown in Figure 5. Due to the small size of this object, it is likely irregularly shaped with a double-peaked rotational lightcurve, so we consider the rotation period of 2012 TW236 to be 10.950 ± 0.003 hours, to our knowledge the first measured value for this object.

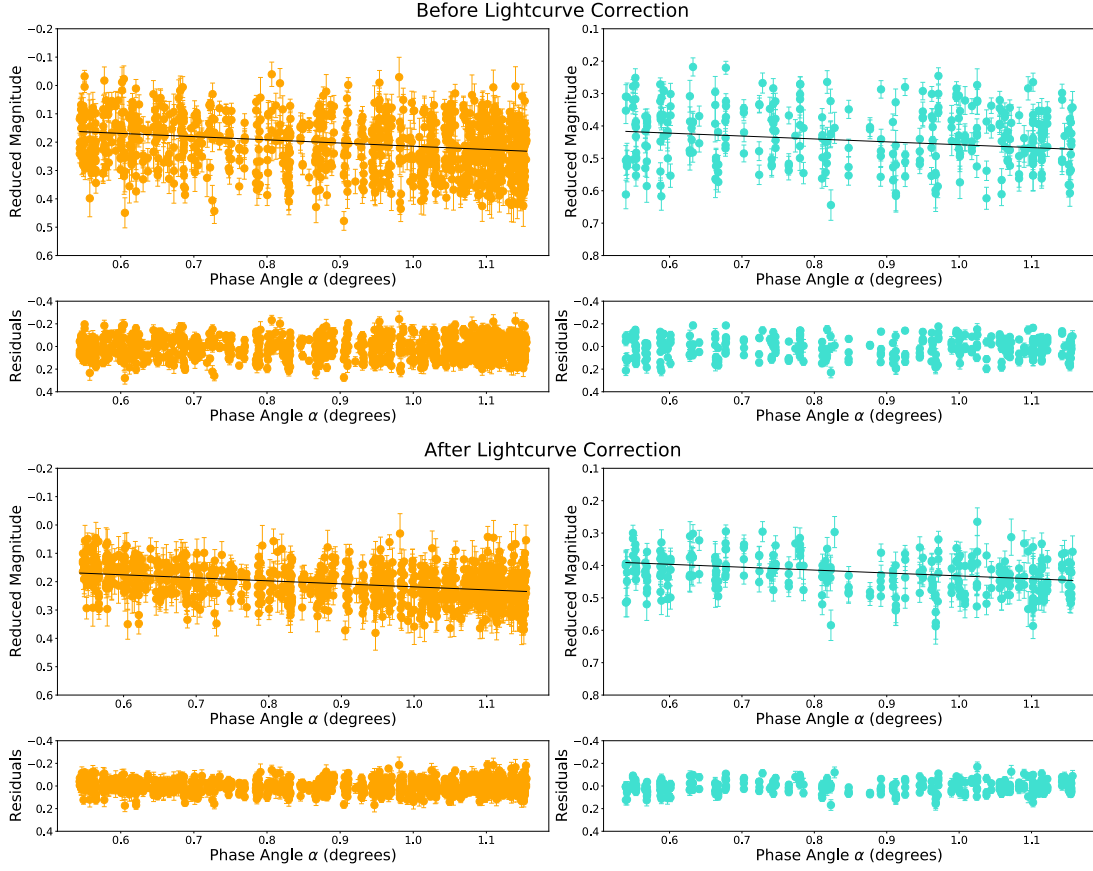


Figure 6. c and o phase curves of Haumea, before (upper plots) and after (lower plots) correction for rotational modulation. Linear best-fit functions plotted as black line, with residuals from the fit displayed beneath each plot.

Table 4. Changes in phase coefficient and absolute magnitude in each ATLAS filter for objects whose datasets were corrected for rotational lightcurve.

Name	β_c before lightcurve correction (mag/deg)	β_c after lightcurve correction (mag/deg)	β_o before lightcurve correction (mag/deg)	β_o after lightcurve correction (mag/deg)
(134340) Pluto	0.045 ± 0.001	0.047 ± 0.001	0.0460 ± 0.006	0.0444 ± 0.006
(136108) Haumea	0.056 ± 0.016	0.090 ± 0.016	0.113 ± 0.010	0.106 ± 0.011
(944) Hidalgo	0.0324 ± 0.0003	0.0318 ± 0.0003	0.0301 ± 0.0002	0.0316 ± 0.0001
(347449) 2012 TW236	0.042 ± 0.005	0.049 ± 0.005	0.038 ± 0.008	0.048 ± 0.008
Name	H_c before lightcurve correction (mag/deg)	H_c after lightcurve correction (mag/deg)	H_o before lightcurve correction (mag/deg)	H_o after lightcurve correction (mag/deg)
(134340) Pluto	-0.7305 ± 0.0015	-0.7313 ± 0.0014	-1.1542 ± 0.0007	-1.1534 ± 0.0007
(136108) Haumea	0.368 ± 0.014	0.343 ± 0.015	0.1011 ± 0.0097	0.1124 ± 0.0097
(944) Hidalgo	11.051 ± 0.009	11.074 ± 0.009	10.776 ± 0.004	10.744 ± 0.004
(347449) 2012T W236	12.549 ± 0.041	12.437 ± 0.042	12.18 ± 0.05	12.12 ± 0.05

Table 5. Rotation Period obtained from ATLAS datasets in o filter and combined filters.

Name	P	P_{final}	Filter(s)	ΔM_c	ΔM_o	Literature P	Literature ΔM	Source
	(hr)	(hr)		(mag)	(mag)	(hr)	(mag)	
(134340) Pluto	153.28 ± 0.65	153.28 ± 0.65	o	0.100 ± 0.004	0.080 ± 0.002	153.2328 ± 0.0048	0.120 ± 0.006	B18
(136108) Haumea	1.95767 ± 0.0001	3.91534 ± 0.00019	o	0.19 ± 0.01	0.205 ± 0.004	3.915341 ± 0.000005	0.28 ± 0.02	SS17
(944) Hidalgo	5.031 ± 0.004	10.06 ± 0.009	o	0.101 ± 0.031	0.237 ± 0.014	10.0630 ± 0.0003	0.48	W97
(347449) 2012 TW236	5.4749 ± 0.0015	10.950 ± 0.003	c and o combined	0.444 ± 0.072	0.568 ± 0.116

References—Rotational period/amplitude sources: B18: [Benecchi et al. \(2018\)](#), SS17: [Santos-Sanz et al. \(2017\)](#), W97: [Wisniewski et al. \(1997\)](#).

We phase-fold the datasets of Pluto, Haumea, Hidalgo, and 2012 TW236 in both filters to their selected rotation period value. We fit a sinusoid of period equal to the chosen rotation period value to the data using the *lmfit* Python package ([Newville et al. 2014](#)), weighted by the uncertainty of each magnitude. This fitted function is subtracted off the reduced magnitude data to eliminate the rotational modulation, and remove any outlying data in the corrected dataset to 3-sigma. The linear phase curve model for the object is refitted again on the corrected data to measure the phase coefficient and absolute magnitude, corrected for the effect of the object’s rotation on its axis. The effect of correcting for an object’s rotational lightcurve is illustrated in Figure 6, showing the significant decrease in spread of the data about the best fitting linear phase curve function. The root mean square values of the residuals to the best-fitting linear function decrease from 0.096 mag to 0.066 mag in the c filter and from 0.093 mag to 0.057 mag in the o filter when the effects of Haumea’s rotational lightcurve is removed. Table 4 lists the phase coefficient and absolute magnitude values for each object for which rotational modulation was corrected, before and after correction. Table 5 lists the amplitudes of the best-fitting sinusoid lightcurve function in both c and o , the uncertainty being calculated from the covariance matrix of the resulting fit. We note that our amplitudes of rotational modulation differ significantly both between filters and from those in literature, though the large uncertainties in ATLAS reduced magnitudes are a possible cause of this.

5.4. Cometary Activity Search

The Centaur and JFC populations contain objects known to exhibit cometary activity ([Lowry et al. 2008](#); [Peixinho et al. 2020](#), and references therein). It is thus plausible that some objects in our sample may have exhibited activity, forming a coma which may partly or fully obscure an object’s surface from direct observation. This would brighten the object’s apparent magnitude, and could alter an object’s phase curve for a period of time. Given the number of datapoints per object, we can use the ATLAS phase curves to search for deviations that may be indicative of possible cometary outgassing or dust production. To search for cometary outbursts, we select for observations that were significantly brighter than predicted from the measured phase curve. We assume that most of an object’s data are taken from epochs of (relative) quiescence potentially punctuated by shorter epochs of activity or outbursts. We consider this assumption to be valid as most of our objects exhibit reduced magnitudes which are consistent in value across separate apparitions. We subtract the best-fitting phase curve function from the dataset (corrected for rotational lightcurve if possible), and select observations brighter than 2σ from the object’s median brightness across the ATLAS baseline.

Active epochs of Centaurs and JFCs exhibit timescales ranging from weeks to years ([Peixinho et al. 2020](#), and references therein). Such activity would manifest as a series of bright observations across consecutive nights. To detect such cometary activity, we utilize the ability of ATLAS to observe a given target multiple times per night, and select nights containing at least 3 observations, of which $\geq 75\%$ have magnitudes brighter than 2σ from the object’s median brightness. We term such nights of observations ‘bright nights’ henceforth. We further analyse these bright nights to determine if cometary activity is the source of the brightening. We note that objects may exhibit activity which do not produce short increases in brightness, and we would not be able to detect this activity using the described algorithm. To detect any such lower-level cometary activity, we consider only observations whose phase-corrected

reduced magnitude lie $<2\sigma$ from the object’s sigma-clipped median brightness. We consider each datapoint in turn, and bin all data taken 30 days after each observation. If at least 14 observations (the approximate average number of ATLAS exposures per week) are taken in any given interval, we consider the median brightness of all data in that interval. If the binned median brightness exceeds the object’s sigma-clipped median brightness by 0.2 mag and 1 standard deviation of the binned data, we consider all data in this interval to be a long outburst. We remove any data which corresponded to epochs of cometary activity from the datasets and reapply the phase curve fitting algorithm to the remaining data. If any instance of cometary activity is found to extend over time, we remove all data in both filters that falls within the time range of the activity.

5.5. HG_1G_2 Model

Several objects in our sample were observed across phase angle ranges comparable to those of main belt asteroids. This allowed us to fit their data from ATLAS with phase curve functions used for these asteroids. The resulting best-fit parameters for our sample could then be compared to those of the asteroid population. We utilize the three-parameter HG_1G_2 phase curve model developed by Muinonen et al. (2010), where H is the absolute magnitude of the phase curve, and G_1 and G_2 both quantify the slopes of the phase angle functions that govern the overall phase curve shape, analogous to the linear phase coefficient β . We utilize this function as per the findings of Mahlke et al. (2021) that taxonomic complexes could be distinguished using the HG_1G_2 function applied to ATLAS data. Mahlke et al. (2021) also found the related HG_{12}^* asteroid phase curve function (Penttilä et al. 2016) failed to distinguish between complexes for ATLAS data, thus we do not apply the HG_{12}^* function to our data. We select only phase curves in a given filter to fit with the HG_1G_2 model which satisfy the following criteria:

1. Observations of $\alpha \geq 12$ deg, to ensure we are sampling the section of the phase curve where curvature becomes significant and the accuracy of linear fits is reduced.
2. Phase curves must contain ≥ 35 datapoints at phase angles $0 \leq \alpha \leq 5$ deg, to ensure we have sufficient sampling of the region where the opposition surge can become significant, which may affect the profile of the fitted phase curve model.

The o filter phase curves of Narcissus, Hidalgo, and 2014 QA43, and the c filter phase curve of Hidalgo satisfy these criteria. We apply the HG_1G_2 model to the reduced magnitude values of these datasets using the HG_1G_2 function from the *Python* photometry module *sppy.photometry* (Mommert et al. 2019). We use a Monte Carlo algorithm to measure the absolute magnitude and G_1 and G_2 parameters, generating 10^5 synthetic phase curves by varying each reduced magnitude value by a random fraction of its associated uncertainty (assuming a normal uncertainty distribution) and fitting the HG_1G_2 model to each synthetic dataset. The final values for H , G_1 , and G_2 are the median of the resulting distribution of all 10^5 values of each parameter, with their associated uncertainties being half of the range between the values which enclose 95% of all values in the distribution, yielding 2σ uncertainties. If an object’s data satisfy the requirements for fitting with the HG_1G_2 , we retroactively use the resulting fit instead of the linear model for eliminating phase angle dependence when searching for rotation periods and cometary activity in the full dataset. For the object Narcissus, due to near-identical resulting chi-square values, we use both the linear and HG_1G_2 fits when searching for rotation period and cometary activity, finding that the choice of fitted function has no effect on the results yielded for Narcissus by either algorithm.

6. RESULTS AND DISCUSSION

6.1. Linear Phase Coefficients - Full Phase Angle Range

We measured the linear phase coefficient β and absolute magnitude H in both ATLAS c and o filters for all 18 objects in our sample across the full range of phase angles spanned by each dataset (excluding opposition surges at $\alpha < 0.1$ deg). Table 6 lists our measured β and H values and 2σ errors for all objects in our sample across the full phase angle range. Figures for all c and o ATLAS phase curves and the 2-dimensional (2D) histograms of the fitted phase curve parameters are shown in Figure 4 and its online Figure set. Linear fits applied to the full range of phase angles spanned by the data were used to correct for variability due to object rotation and cometary activity for all objects, apart from the o filter datasets of Narcissus and 2014 QA43 and the c and o filter datasets of Hidalgo which were corrected using the HG_1G_2 function. Four such objects - 2012 TW236, 2014 QA43, 2016 ND21, and Narcissus - have datasets which extend to phase angles beyond $\alpha \sim 10$ deg where non-linearity could become significant, but

the small number of objects this applies to means we consider a linear fit suitable for variability correction. However, for the remainder of our analysis, including a comparison to the Kuiper belt and its associated populations, we restrict ourselves to measuring phase coefficients and absolute magnitudes for a fixed phase angle range of $0.1 \leq \alpha \leq 6$ deg, as detailed in section 6.2.

Table 6. Linear phase coefficients β and absolute magnitudes H for all objects in our sample in both ATLAS broadband filters c and o , measured over the full range of phase angles for each filter dataset, with associated 2σ uncertainties, with phase angle range over which the parameters were measured in each filter. Parameter values measured across the maximum range of phase angles in each filter, with data corrected for rotational lightcurves and cometary activity wherever possible.

Object	β_c (mag/deg)	H_c (mag)	α range (c filter) (deg)	N_c	β_o (mag/deg)	H_o (mag)	α range (o filter) (deg)	N_o	Light curve	Cometary activity
KBOs										
(136199) Eris	0.043 ± 0.088	-1.012 ± 0.042	$0.1206-0.6058$	239	0.016 ± 0.043	-1.307 ± 0.018	$0.1214-0.6068$	738	No	No
(136108) Haumea	0.089 ± 0.017	0.343 ± 0.014	$0.5397-1.1567$	313	0.106 ± 0.01	0.112 ± 0.01	$0.544-1.1548$	1043	Yes	No
(38628) Huya	-0.015 ± 0.085	4.974 ± 0.096	$0.5515-1.9664$	68	0.058 ± 0.031	4.476 ± 0.04	$0.5394-2.0139$	340	No	No
(136472) Makemake	0.005 ± 0.015	0.107 ± 0.013	$0.5209-1.1062$	353	0.034 ± 0.009	-0.247 ± 0.008	$0.5193-1.1087$	1088	No	No
(90482) Orcus	0.18 ± 0.065	2.238 ± 0.059	$0.4008-1.2082$	271	0.07 ± 0.04	2.07 ± 0.037	$0.4045-1.2084$	541	No	No
(134340) Pluto ^a	0.045 ± 0.001	-0.728 ± 0.002	$0.1085-1.7313$	323	0.0448 ± 0.0006	-1.1536 ± 0.0007	$0.1152-1.7362$	886	Yes	No
(50000) Quaoar	0.029 ± 0.065	2.792 ± 0.057	$0.1964-1.341$	177	0.075 ± 0.028	2.221 ± 0.025	$0.1925-1.3402$	590	No	No
Centaur										
(459865) 2013 XZ8	0.026 ± 0.017	9.937 ± 0.087	$2.8174-6.8551$	127	0.036 ± 0.011	9.524 ± 0.052	$2.1459-6.9036$	329	No	No
(54598) Btenor	0.058 ± 0.025	7.586 ± 0.07	$1.3222-4.0222$	172	0.062 ± 0.014	7.248 ± 0.041	$1.3103-4.0452$	431	No	No
(10199) Chariklo	0.035 ± 0.019	6.939 ± 0.044	$0.1041-3.6314$	170	0.049 ± 0.01	6.477 ± 0.022	$0.1535-3.5772$	454	No	No
(2060) 95P/Chiron	0.093 ± 0.011	5.69 ± 0.023	$0.2194-3.093$	234	0.097 ± 0.006	5.433 ± 0.011	$0.1688-3.1055$	834	No	Yes
JFCs										
(347449) 2012 TW236	0.049 ± 0.005	12.437 ± 0.042	$2.0318-17.0886$	69	0.048 ± 0.008	12.123 ± 0.05	$1.9453-14.469$	58	Yes	No
(501585) 2014 QA43	0.063 ± 0.015	11.781 ± 0.131	$3.7953-11.9905$	81	0.064 ± 0.005	11.379 ± 0.041	$1.2204-11.8886$	270	No	Yes ^b
2016 ND21	0.032 ± 0.005	12.635 ± 0.043	$0.1533-14.7265$	91	0.048 ± 0.003	12.063 ± 0.027	$2.0524-15.0726$	333	No	No
(944) Hidalgo	0.0318 ± 0.0003	11.074 ± 0.009	$2.1269-30.5594$	178	0.0316 ± 0.0002	10.744 ± 0.004	$1.1296-30.5823$	730	Yes	No
(37117) Narcissus	0.048 ± 0.003	13.573 ± 0.023	$2.5505-18.5841$	69	0.044 ± 0.002	13.161 ± 0.021	$1.5666-18.3289$	204	No	No
Transition Objects										
(349933) 2009 YF7	0.032 ± 0.018	11.117 ± 0.099	$1.9905-8.5739$	110	0.036 ± 0.01	10.747 ± 0.064	$1.9827-8.9607$	285	No	No
(60558) 174P/Echeclus	0.083 ± 0.008	9.804 ± 0.039	$0.9073-8.6663$	111	0.064 ± 0.003	9.403 ± 0.015	$0.383-9.5528$	363	No	Yes

^a Values are for the Pluto/Charon system, whose components cannot be resolved at the ATLAS pixel scale.

^b While we do not detect any confirmed instance of cometary activity for 2014 QA43, we nevertheless remove all data classified by our activity search algorithm as occurring during an instance of sustained brightening. It is not clear if this brightening is due to cometary activity not visible in the ATLAS images or due to changing aspect angle.

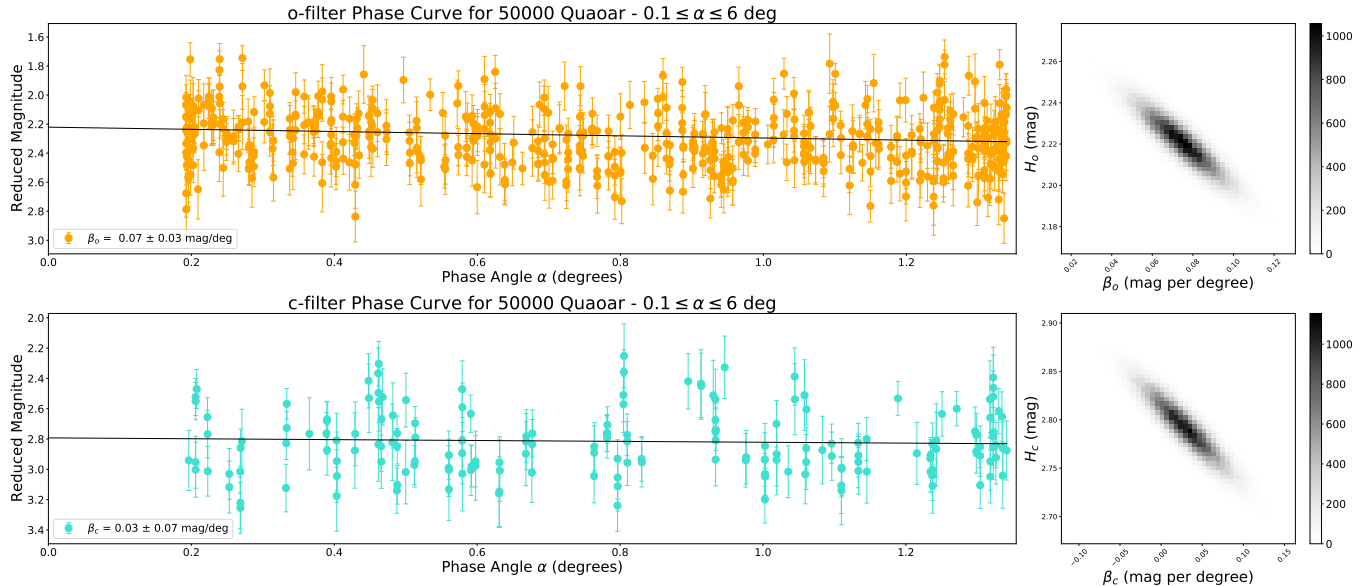


Figure 7. Linear fit to phase curve of (50000) Quaoar in ATLAS *o* and *c* filters for data in phase angle range $0.1 \leq \alpha \leq 6$ deg. Best fit function extended to $\alpha = 0$ deg for ease of viewing the extrapolated absolute magnitude value and any potential opposition surge. The complete figure set (13 images) is available in the online published version of the paper.

6.2. Linear Phase Coefficients - Limited Phase Angle Range

The objects in our sample span semimajor axes of $5.7 \text{ au} \leq a \leq 68.1 \text{ au}$, resulting in a wide range of maximum phase angles observable from Earth. ATLAS observations thus sample different sections of the phase curves depending on an object’s heliocentric distance. To compare phase curves over a fixed range of phase angle, we restrict our datasets (corrected for rotational modulation and cometary activity where possible and excluding data at $\alpha \leq 0.1$ deg) to include only observations taken at phase angles $\alpha \leq 6$ deg, and consider only objects with >50 datapoints in this range in both *c* and *o*. We apply our methods to the resulting phase curves of 13 objects. The resulting absolute magnitudes and phase coefficients in *c* and *o* are listed in Table 7. Comparing the resulting values to those measured over the maximum phase angle range, we find that the phase coefficient and absolute magnitude values change beyond 2σ error bars only for the Transition Objects Echeclus and 2009 YF7 in the *c* filter. Figures for all *c* and *o* ATLAS phase curves for data in phase angle range $0.1 \leq \alpha \leq 6$ are shown in Figure 7 and its online Figure set.

We note that our β values differ by $>2\sigma$ between the ATLAS filters for many objects. Significant variation of β with wavelength has been previously reported by several multi-filter phase curve studies of Centaurs and KBOs (Buratti et al. 2003; Rabinowitz et al. 2007; Schaefer et al. 2009; Alvarez-Candal et al. 2016; Ayala-Loera et al. 2018; Alvarez-Candal et al. 2019). Figure 8 shows the ATLAS β values compared to those from the literature in the Johnson-Cousins *BVRI* photometric system, for which the ATLAS filters *c* and *o* exhibit significant overlap in wavelength range with *B* and *V* filters (*c* filter) and *R* and *I* filters (*o* filter), respectively. Though the ATLAS β values often differ in value from the literature, for most objects they overlap within the 2σ error bars or lie between the extremes of the range of the literature values for a given object. Our ATLAS linear phase coefficients are consistent with those from the literature, as expected, and we attribute any disparity to be due to different wavelength ranges of the filters of the ATLAS and Johnson-Cousins photometric systems. We also note that our measured phase coefficient and absolute magnitudes for Pluto are those of the Pluto-Charon system, the components of which cannot be resolved at the ATLAS pixel scale.

Figure 9 shows the best-fitting linear phase curve models for all objects in our sample, divided by dynamical class and photometric filter. The β values indicate relatively flat phase curves across our entire sample, with values ranging from -0.01 to 0.18 mag/deg in *c*, and 0.02 to 0.106 mag/deg in *o*. Such flat phase curves have been previously observed for several JFCs, Centaurs, and Pluto-sized KBOs (Rabinowitz et al. 2006, 2007; Kokotanekova et al. 2017, 2018; Verbiscer et al. 2022) and are thought to be indicative of low-albedo organic-rich Centaur and JFC surfaces (Nelson et al. 2000; Shkuratov et al. 2002; Cruikshank & Dalle Ore 2003; Rabinowitz et al. 2007) and high-albedo

Table 7. Linear phase coefficients β and absolute magnitudes H for all objects with >50 data points recorded at phase angles $0.1 \leq \alpha \leq 6$ deg in both ATLAS broadband filters c and o , with associated 2σ uncertainties, and number of data points N at $0.1 \leq \alpha \leq 6$ deg in each ATLAS filter.

Object	β_c (mag/deg)	H_c	N_c ($\alpha \leq 5$ deg)	β_o (mag/deg)	H_o	N_o ($\alpha \leq 5$ deg)	Light curve correction?	Cometary activity correction?
KBOs								
(136199) Eris	0.043 ± 0.088	-1.012 ± 0.042	239	0.016 ± 0.043	-1.307 ± 0.018	738	No	No
(136108) Haumea	0.089 ± 0.017	0.343 ± 0.014	313	0.106 ± 0.01	0.112 ± 0.01	1043	Yes	No
(38628) Huya	-0.015 ± 0.085	4.974 ± 0.096	68	0.058 ± 0.031	4.476 ± 0.040	340	No	No
(136472) Makemake	0.005 ± 0.015	0.107 ± 0.013	353	0.034 ± 0.009	-0.247 ± 0.008	1088	No	No
(90482) Orcus	0.18 ± 0.065	2.238 ± 0.059	271	0.07 ± 0.04	2.07 ± 0.037	541	No	No
(134340) Pluto ^a	0.045 ± 0.001	-0.728 ± 0.002	323	0.0448 ± 0.0006	-1.1536 ± 0.0007	886	Yes	No
(50000) Quaoar	0.029 ± 0.065	2.792 ± 0.057	177	0.075 ± 0.028	2.221 ± 0.025	590	No	No
Centaur								
(459865) 2013 XZ8	0.024 ± 0.023	9.948 ± 0.105	85	0.031 ± 0.016	9.546 ± 0.069	236	No	No
(54598) Bienor	0.058 ± 0.025	7.586 ± 0.07	172	0.062 ± 0.014	7.248 ± 0.041	431	No	No
(10199) Chariklo	0.035 ± 0.019	6.939 ± 0.044	170	0.049 ± 0.01	6.477 ± 0.022	454	No	No
(2060) 95P/Chiron	0.093 ± 0.011	5.69 ± 0.023	234	0.097 ± 0.006	5.433 ± 0.011	834	No	Yes
Transition Objects								
(60558) Echeclus	0.094 ± 0.012	9.769 ± 0.048	81	0.069 ± 0.006	9.394 ± 0.018	252	No	Yes
(349933) 2009 YF7	0.113 ± 0.033	10.768 ± 0.159	85	0.067 ± 0.027	10.611 ± 0.125	137	No	No

^a Values are for the Pluto/Charon system, whose components cannot be resolved at the ATLAS pixel scale.

KBO surfaces covered in granular volatile ices (Brown et al. 2005; Licandro et al. 2006; Rabinowitz et al. 2006, 2007; Trujillo et al. 2007). Furthermore, we find that for both the c and o filters, the phase coefficient values of the Centaurs and Transition Objects all fall in the same range as those of the KBO population when measured across the same phase angle range $0.1 \leq \alpha \leq 6$ deg. All but one of our sample exhibit positive phase coefficient slopes in both ATLAS filters. Huya exhibits a marginally negative phase coefficient in the c filter, as shown in Figure 10 but is consistent within 2σ of having a flat or positive slope. Alvarez-Candal et al. (2016); Ayala-Loera et al. (2018); Alvarez-Candal et al. (2019) reported negative phase coefficients for several objects in their sample, including Chiron, Eris, Haumea, Huya, and Makemake. $\beta < 0$ would imply an unphysical dimming near opposition. Alvarez-Candal et al. (2016) and Ayala-Loera et al. (2018) speculated this effect may be due to unidentified ring systems, epochs of cometary activity, or poorly corrected rotational modulation. We instead measure phase coefficient values for these objects which are either positive slopes or consistent with positive slopes to within 2σ . Furthermore, Huya’s negative c filter phase coefficient is derived from the second sparsest dataset in our sample of $N_c = 68$ observations, comparable in size to the V filter dataset from Ayala-Loera et al. (2018) ($N_V = 45$) which also yielded a negative phase coefficient value. This tendency towards positive β values with increasing dataset size suggests negative phase coefficient values are most likely due to small datasets with large scatter which are unable to sufficiently sample the phase curve profile, and not a real property of these objects.

6.3. Correlations

We explore potential correlations between phase coefficients β_c and β_o , absolute magnitudes H_c and H_o , color index $H_c - H_o$, and relative phase coefficients $\beta_c - \beta_o$ derived from the ATLAS phase curves. We analyse parameter values measured across the phase angle range $0.1 \leq \alpha \leq 6$ deg to ensure all parameters are measured over the same region of the phase curve. We make use of the Spearman rank correlation test to search for monotonic relationships between pairs of variables, using the *spearmanr* function from the python module *scipy* (Virtanen et al. 2020). The *spearmanr* function calculates two parameters. The first is the Spearman rank correlation coefficient, r_s , which quantifies the strength and direction of any detected monotonic relationship between two variables; $|r_s| \rightarrow 1$ defines a strong correlation, whereas $r_s \approx 0$ implies no correlation. The second parameter is the null hypothesis probability value of that correlation, or p-value, P_{r_s} , which quantifies the probability that any detected correlation is derived from

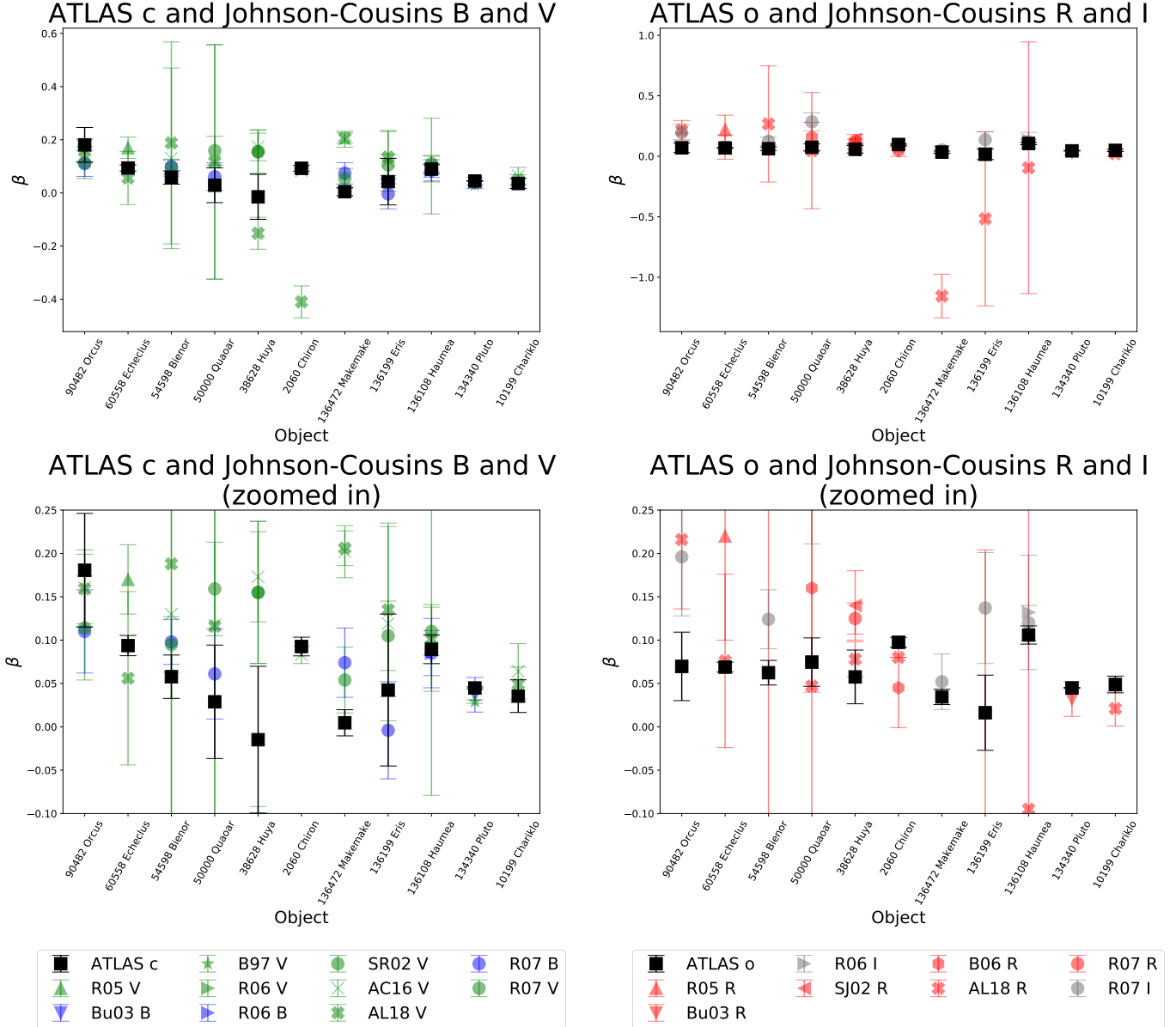


Figure 8. *Upper plots:* Linear phase coefficients in ATLAS *c* (left, black squares) and *o* (right, black squares), calculated from the phase angle range $0.1 \leq \alpha \leq 6$ deg, with literature values in Johnson-Cousins broadband filters (blue: *B*, green: *V*, red: *R*, grey: *I*) with which ATLAS filters exhibit significant overlap. *Lower plots:* Upper plots magnified for clarity. AC16: Alvarez-Candal et al. (2016), AL18: Ayala-Loera et al. (2018), Bu03: Buratti et al. (2003), B97: Buie et al. (1997), B06: Bagnulo et al. (2006), R05: Rousselot et al. (2005), R06: Rabinowitz et al. (2006), R07: Rabinowitz et al. (2007), SJ02: Sheppard & Jewitt (2002), SR02: Schaefer & Rabinowitz (2002).

an inherently uncorrelated distribution of data. We note however that the Spearman rank correlation test itself does not consider uncertainties in the analysed variables. To account for this, for every parameter pair tested, we perform a Monte Carlo simulation on the parameter values. For each data point, we vary the nominal value within associated uncertainties, assuming every uncertainty follows a normal distribution with a standard deviation equal to the nominal value of the uncertainty itself, perform the rank statistic on the resulting synthetic values, and repeat 10^5 times. We accumulate all the associated p-values and calculate the percentage of simulations for which $P_{r_s} > 0.05$ i.e. we could not rule out an uncorrelated population to 95% probability. We consider a correlation to exist if $|r_s| \geq 0.5$ and $< 5\%$ of simulations return $P_{r_s} > 0.05$. A correlation that satisfies one of these criteria is considered tentative, and we reject any correlation if neither is satisfied or $P_{r_s} > 95\%$. We apply the Spearman rank correlation test to our full sample

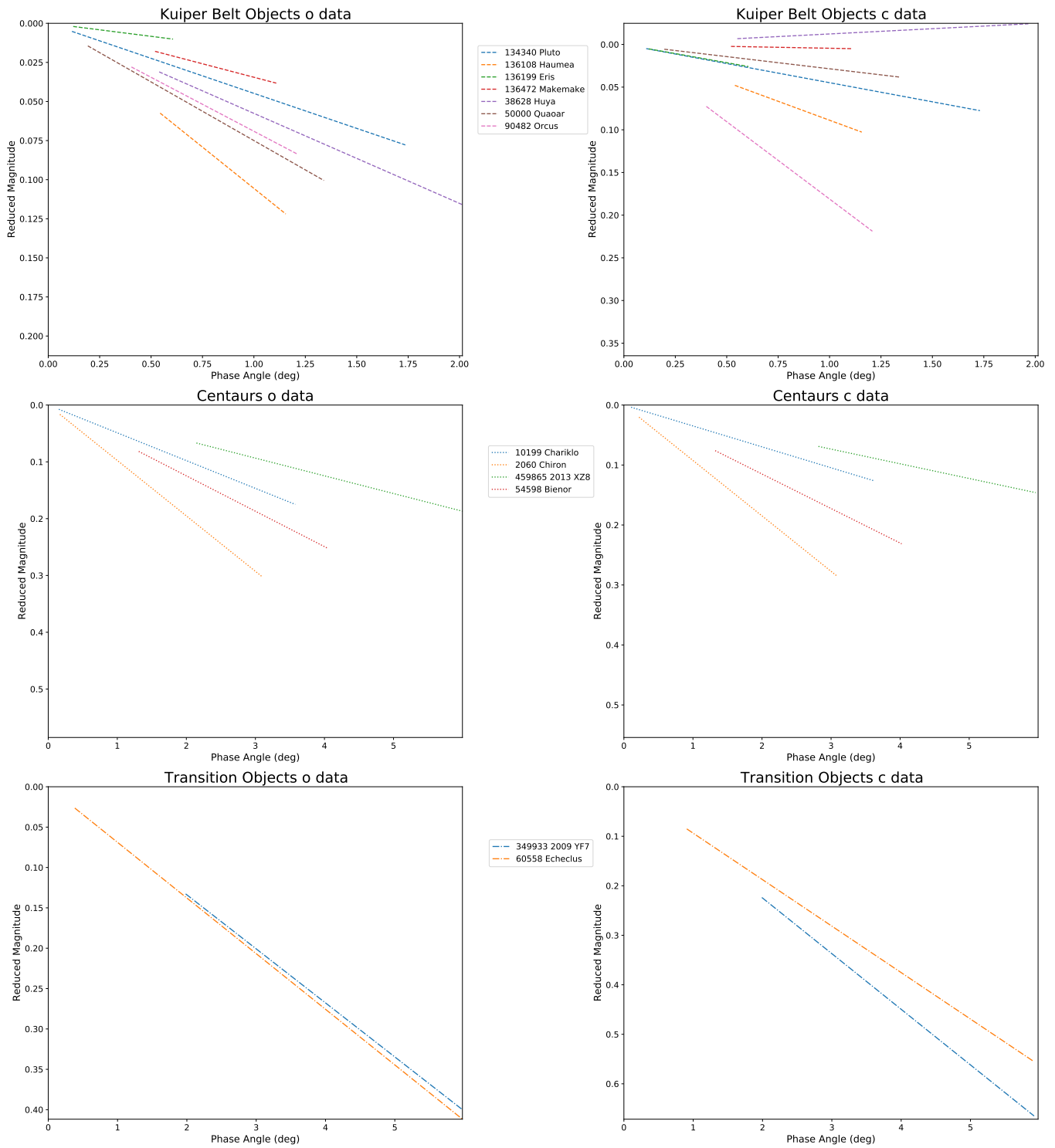


Figure 9. Best-fit linear phase curves for all objects in our sample, divided by filter (*c* filter left, *o* filter right) and dynamical classification, spanning the phase angle range of each dataset in each filter. All phase curves are normalized to 0 mag at opposition ($\alpha = 0$ deg) to enable comparison of slope values.

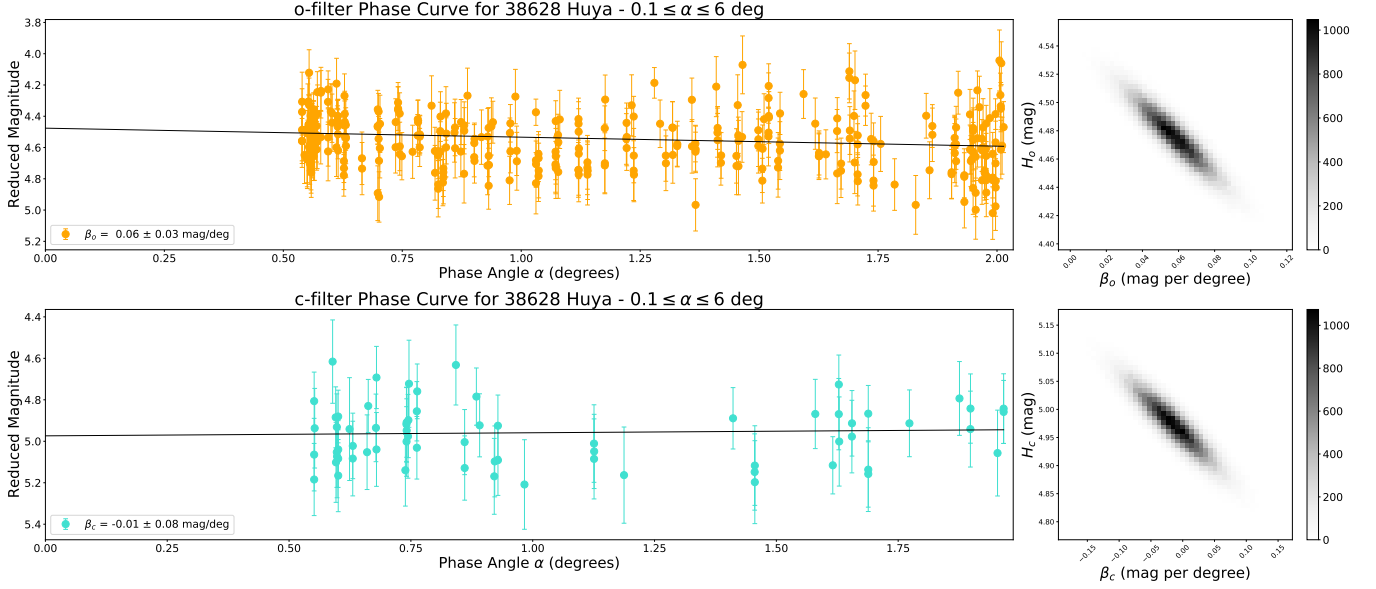


Figure 10. Linear fit to phase curve of (38628) Huya in c and o filters, with 2D histograms showing density plot of error distributions of linear phase coefficient and absolute magnitude. Best fit function extended to $\alpha = 0$ deg for ease of viewing any potential opposition surge. Note the nominally negative β_c value, whose associated uncertainty nevertheless makes it consistent with a flat sloped phase curve, consistent with atmosphereless surface reflectance.

and subsamples: Centaurs/JFCs/Transition Objects; KBOs; dwarf planets ($H \leq 3$); and non-dwarf planet objects from the KBO, Centaur, JFC, and Transition Object populations ($H > 3$). Figure 11 shows plots of the tested ATLAS parameters for the full object sample, the Centaurs, JFCs, Transition Objects, the KBOs, the dwarf planets, and the non-dwarf planet objects in our sample.

Table 8 lists the parameters from our Spearman rank correlation tests. We find no strong correlations between β_c and H , β_o and H , and β_o and $H_c - H_o$ for the full sample and all sub-populations. However, we find a tentative negative correlation between β_c and $H_c - H_o$ for the full sample and all sub-populations as we cannot reject the null hypothesis to $>95\%$ confidence. A tentative negative correlation between β_o and $H_c - H_o$ is also found for the Centaur/JFC/Transition Object and non-dwarf planet populations. We also find a tentative negative correlation between $\beta_c - \beta_o$ and $H_c - H_o$ for the full sample, the KBO population, and the non-dwarf planet population, yet no significant correlation between these parameters for the dwarf planet population, and a tentative correlation that can almost be ruled out to 95% confidence for the Centaur/JFC/Transition Objects sub-population. No strong correlation is identified for any tested parameter pair. We also find no significant change in correlation results when applying or correlation search algorithm to parameter values derived from the full phase angle range.

We also apply our algorithm to the data of Ayala-Loera et al. (2018), who reported phase coefficients and absolute magnitudes for 114 objects in Johnson-Cousins V and R filters, which exhibit overlap in wavelength range with ATLAS c and o . We select only objects from their study with β values consistent with positive to within 2σ and divide their object sample according to our definitions. Table 9 lists the results from applying our algorithm to their data. For β and H , we find tentative negative correlations for the Centaurs/JFCs/Transition Objects sub-population in both the V and R filters. For β and $H_V - H_R$, we find no correlation in V for any sub-population, yet find a tentative positive correlation for the Centaurs/JFCs/Transition Objects and the dwarf planets sub-population. For $\beta_V - \beta_R$ and $H_V - H_R$, we find highly significant negative correlations for the full sample, the KBOs, and the non-dwarf planet sub-populations.

We find a highly significant negative correlation using data from Ayala-Loera et al. (2018) for objects with phase coefficient values consistent with positive to within 2σ . We also find similar negative correlations with ATLAS data

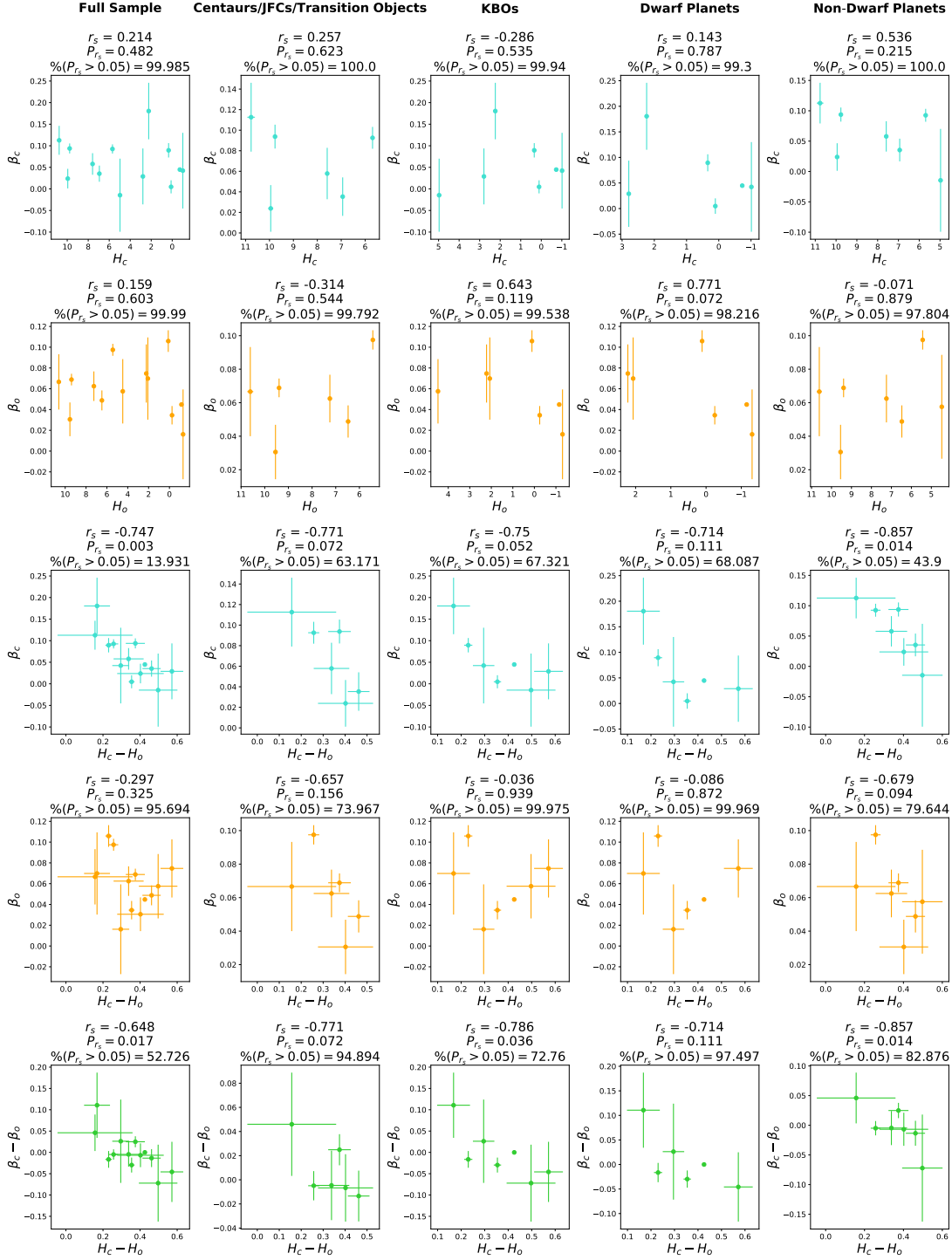


Figure 11. Plots of tested parameter pairs derived from ATLAS observations for our full object sample (first column); Centaurs, JFCs, and Transition Objects (second column); KBOs (third column); dwarf planets (fourth column); and non-dwarf planets (last column).

for the full sample, the KBOs, and the non-dwarf planets sub-populations. However, these correlations are tentative, and an inherently uncorrelated distribution cannot be ruled out to 95% confidence. Jackknife re-sampling of the [Ayala-Loera et al. \(2018\)](#) sample, using sub-sample sizes of $N = 13$ (for the full ATLAS sample) and $N = 7$ (for both the KBO and non-dwarf planet sub-populations), yields no correlation for 16.3% of simulations. Thus the difference in

Table 8. Results of correlation investigation using ATLAS data in phase angle range $0.1 \leq \alpha \leq 6$ deg. Spearman rank correlation coefficients r_s , associated null hypothesis probability values P_{r_s} , percentage of Monte Carlo simulations where $P_{r_s} > 0.05$ (i.e. we cannot reject a random distribution to 95% confidence), and number of datapoints analysed for correlation tests between phase curve parameters using ATLAS data.

Parameters	r_s	P_{r_s}	% Simulations with $P_{r_s} > 0.05$	N	Correlation?
Full Sample					
β_c vs H_c	0.214	0.482	99.985	13	No
β_o vs H_o	0.159	0.603	99.99	13	No
β_c vs $H_c - H_o$	-0.747	0.003	13.931	13	Tentative
β_o vs $H_c - H_o$	-0.297	0.325	95.694	13	No
$\beta_c - \beta_o$ vs $H_c - H_o$	-0.648	0.017	52.726	13	Tentative
Centaur/JFCs/Transition Objects					
β_c vs H_c	0.257	0.623	100.0	6	No
β_o vs H_o	-0.314	0.544	99.792	6	No
β_c vs $H_c - H_o$	-0.771	0.072	63.171	6	Tentative
β_o vs $H_c - H_o$	-0.657	0.156	73.967	6	Tentative
$\beta_c - \beta_o$ vs $H_c - H_o$	-0.771	0.072	94.894	6	Tentative
KBOS					
β_c vs H_c	-0.286	0.535	99.94	7	No
β_o vs H_o	0.643	0.119	99.538	7	No
β_c vs $H_c - H_o$	-0.75	0.052	67.321	7	Tentative
β_o vs $H_c - H_o$	-0.036	0.939	99.975	7	No
$\beta_c - \beta_o$ vs $H_c - H_o$	-0.786	0.036	72.76	7	Tentative
Dwarf Planets					
β_c vs H_c	0.143	0.787	99.3	6	No
β_o vs H_o	0.771	0.072	98.216	6	No
β_c vs $H_c - H_o$	-0.714	0.111	68.087	6	Tentative
β_o vs $H_c - H_o$	-0.086	0.872	99.969	6	No
$\beta_c - \beta_o$ vs $H_c - H_o$	-0.714	0.111	97.497	6	No
Non-Dwarf Planets					
β_c vs H_c	0.536	0.215	100.0	7	No
β_o vs H_o	-0.071	0.879	97.804	7	No
β_c vs $H_c - H_o$	-0.857	0.014	43.9	7	Tentative
β_o vs $H_c - H_o$	-0.679	0.094	79.644	7	Tentative
$\beta_c - \beta_o$ vs $H_c - H_o$	-0.857	0.014	82.876	7	Tentative

size between our sample and that of [Ayala-Loera et al. \(2018\)](#) is likely responsible for this discrepancy in correlation certainty. Furthermore, our ATLAS datasets usually have many more observations than those of [Ayala-Loera et al. \(2018\)](#), and are taken in filters of different wavelength ranges. We therefore consider our findings to be consistent with those of [Ayala-Loera et al. \(2018\)](#) and attribute any difference in correlation certainty to be due to differing sample sizes, dataset sizes, and filter wavelength ranges. An increase in the number of objects with phase coefficient and absolute magnitude measurements from datasets comparable to those afforded by ATLAS would allow us to potentially recover this negative correlation between relative phase coefficient - the difference in phase coefficient value between broadband filters of differing wavelength range - and color index.

[Ayala-Loera et al. \(2018\)](#) reported the strong negative correlation between relative phase coefficient and color index as persisting even when their sample was divided by absolute magnitude and semimajor axis. However, their sample was divided by semimajor axis and absolute magnitude at $a = 40$ au and $H = 4.5$, in contrast to our thresholds of $a = 30$ au and $H = 3$. Dividing our sample by the sub-population definitions of [Ayala-Loera et al. \(2018\)](#) using H values calculated from ATLAS data, we find tentative correlations for the $a < 40$ au and $H > 4.5$ subpopulations, and no correlation for the $H < 4.5$ au subpopulation, with the $a > 40$ au population being too small for an accurate rank statistic. Applying our algorithm to their sample divided by their definitions, we also find strong negative correlations between relative phase coefficient and color index for the $H > 4.5$ population and $a > 40$ au population, and tentative negative correlations for the $a < 40$ au population and $H < 4.5$ au populations. Dividing their sample by

Table 9. Results of correlation investigation using data from [Ayala-Loera et al. \(2018\)](#). Spearman rank correlation coefficients r_s , associated null hypothesis probability values P_{r_s} , percentage of Monte Carlo simulations where $P_{r_s} > 0.05$ (i.e. we cannot reject a random distribution to 95% confidence), number of datapoints N analysed for correlation tests between phase curve parameters from [Ayala-Loera et al. \(2018\)](#), and if the parameters exhibit a correlation.

Parameters	r_s	P_{r_s}	% Simulations with $P_{r_s} > 0.05$	N	Correlation?
Full Sample					
β_V vs H_V	-0.278	0.005	18.208	100	No
β_R vs H_R	-0.176	0.081	77.217	99	No
β_V vs $H_V - H_R$	-0.219	0.037	81.36	91	No
β_R vs $H_V - H_R$	0.408	0.0	10.796	91	No
$\beta_V - \beta_R$ vs $H_V - H_R$	-0.747	0.0	0.133	91	Yes
Centaur/JFCs/Transition Objects					
β_V vs H_V	-0.508	0.026	14.087	19	Tentative
β_R vs H_R	-0.521	0.022	13.153	19	Tentative
β_V vs $H_V - H_R$	-0.449	0.054	90.363	19	No
β_R vs $H_V - H_R$	-0.573	0.010	75.758	19	Tentative
$\beta_V - \beta_R$ vs $H_V - H_R$	-0.307	0.201	84.616	19	No
KBOs					
β_V vs H_V	-0.152	0.177	99.297	81	No
β_R vs H_R	-0.110	0.330	99.959	80	No
β_V vs $H_V - H_R$	-0.271	0.022	75.219	72	No
β_R vs $H_V - H_R$	0.418	0.0	19.681	72	No
$\beta_V - \beta_R$ vs $H_V - H_R$	-0.802	0.0	0.248	72	Yes
Dwarf Planets					
β_V vs H_V	0.143	0.787	100.0	6	No
β_R vs H_R	0.6	0.208	99.623	6	No
β_V vs $H_V - H_R$	0.429	0.397	86.778	6	No
β_R vs $H_V - H_R$	0.771	0.072	86.046	6	Tentative
$\beta_V - \beta_R$ vs $H_V - H_R$	-0.714	0.111	96.087	6	No
Non-Dwarf Planets					
β_V vs H_V	-0.241	0.019	56.606	94	No
β_R vs H_R	-0.225	0.031	35.844	93	No
β_V vs $H_V - H_R$	-0.230	0.034	81.014	85	No
β_R vs $H_V - H_R$	0.377	0.0	19.221	85	No
$\beta_V - \beta_R$ vs $H_V - H_R$	-0.745	0.0	0.28	85	Yes

our definitions of sub-populations, we find no correlation for Centaurs/JFCs/Transition Objects or the dwarf planets sub-populations, yet a strong correlation for the KBOs and the non-dwarf planet sub-population which is dominated in number by KBOs. This difference in observed correlation between populations may point to a difference in substructure between the surfaces of these objects, likely caused by an evolutionary effect due to differing insolation. An increased sample size similar to those of [Alvarez-Candal et al. \(2016\)](#), [Ayala-Loera et al. \(2018\)](#) and [Alvarez-Candal et al. \(2019\)](#), with precisions of parameter values comparable to those afforded by the ATLAS datasets, would help to better recover and study this negative correlation between relative phase coefficient and color index, which may in fact be a universal property across different populations of small Solar System objects ([Alvarez-Candal et al. 2022](#)), and confirm the existence of this possible distinction.

6.4. Cometary Activity Search

We searched for instances of cometary activity in the ATLAS datasets for all 18 objects in our sample. Most of our sample show no sign of cometary activity. A small number of objects, namely Chiron, Echeclus, Pluto, and Quaoar exhibit ‘bright nights’ as defined in Section 5.4, suggesting potential cometary outbursts or long-term activity. Table 10 lists the bright observations per object identified by our algorithm as potentially indicative of cometary activity, either in the form of short outbursts or longer-term sustained brightening. We discuss each object below:

Echeclus - we detect three separate instances of bright nights across the ATLAS baseline, as shown in Figure 12. The first, seen in the *c* filter on 2018 January 17 (MJD 58135) and the *o* filter from 2017 December 24 (MJD 58111) to 2018 January 2 (MJD 58120), coincides in time with a previously reported 2017 December outburst (James 2018; Kareta et al. 2019). During this outburst, Echeclus exhibited a fan-shaped coma which remained clearly visible in the ATLAS images for approximately 1 month, as seen in Figure 13. This activity seemed to build to a second outburst observed as two consecutive bright nights, 2018 March 6 (MJD 58183) and 2018 March 8 (MJD 58185). Analysis of the full width half maximum (FWHM) of the PSF of Echeclus during the night of 2018 March 6 (the night during which the PSF of Echeclus was more clearly visible) reveals significant spread compared to those of background stars, as shown in Figure 14. The PSF FWHM of Echeclus compared to that of the background stars for this date are listed in Table 11, indicative of a visible coma. The third instance appears as a single bright night in the *o* filter on 2018 April 9, however analysis of the ATLAS images reveals Echeclus to lie close to a poorly-subtracted background star during this time, as seen in Figure 15, making this a result of background stellar flux contamination, and not a comet-like outburst.

Chiron - we detect two separate instances of bright nights, highlighted in Figure 16. The first is a single bright night at 2016 December 22 (MJD 57744) observed in *c*; visual inspection reveals Chiron lies close to a poorly-subtracted background star, as seen in Figure 15, thus this brightening is due to stellar contamination. The second instance is an increase in brightness constituting three consecutive bright nights starting at 2021 June 18 (MJD 59383), the first three nights of observation of a new apparition of Chiron. No coma or tail is visible in the ATLAS images, and Chiron’s flux signal appears stellar (see Figures 17 and 18 and Table 11), yet this brightness increase exceeds Chiron’s amplitude of rotational modulation. This new epoch of increased activity is reported in Dobson et al. (2021a) and Dobson et al. (2021b). Further analysis of Chiron is beyond the scope of this study, and will be subject of a later paper.

Pluto - we detect two bright nights at 2019 July 5 (MJD 58669) and 2020 October 7 (MJD 59129), highlighted in Figure 19, yet neither are caused by cometary activity. Visual inspection of ATLAS images of each night shows that Pluto is contaminated by background stars, as seen in Figure 15.

Quaoar - we detect a single bright night at 2021 March 22 (MJD 59295), highlighted in Figure 20. We find Quaoar lies close to a poorly-subtracted background star in all observations from this night, as seen in Figure 15, contaminating its photometry.

We also detect two further instances of brightening for both Echeclus and 2014 QA43 which may correspond to long-term activity, described below:

Echeclus - we detect an instance of sustained brightening of 0.2 mag and >1 standard deviation of the data from the sigma-clipped median ranging from 2017 November 10 (MJD 58067) to 2018 February 12 (MJD 58161), as highlighted in Figure 12. This coincides in time with Echeclus’s $>2\sigma$ outburst in 2017 December, and a fan-shaped coma is clearly visible in the ATLAS images during this time, as seen in Figure 13.

2014 QA43 - we detect an instance of brightening ranging in time from 2020 September 16 (MJD 59108) to 2020 December 7 (MJD 59190), spanning a large fraction of the observations from that apparition, as shown in Figure 21. The median phase-corrected reduced magnitude of this apparition is brighter than that of previous years of data by approximately 0.3 mag. Measurements of the FWHM of 2014 QA43 reveals no significant broadening compared to background stars, as seen in Figure 22. It remains unclear if this brightening is due to cometary activity not visible in the images or due to the changing aspect angle of the object.

In conclusion, only Chiron and Echeclus are found to exhibit definite comet-like activity. It is not surprising that we find these objects have been active during the ATLAS survey, as both Chiron (Bus et al. 1988; Luu & Jewitt 1990; Dahlgren et al. 1991; Marcialis & Buratti 1993; Elliot et al. 1995; Lazzaro et al. 1997b; Silva & Cellone 2001; Duffard et al. 2002) and Echeclus (Choi et al. 2006a,b; Jaeger et al. 2011; Rousselot et al. 2016; James 2018; Seccull et al. 2019; Kareta et al. 2019) have well-recorded histories of comet-like activity in the literature. Both these objects have been classified by previous studies as belonging to the Centaur population, members of which have been known to exhibit comet-like outbursts. However, unlike comets, Centaur activity is decoupled from perihelion. The mechanism responsible for cometary activity on Centaurs currently remains elusive at present. Jewitt (2009) found that from a population of 23 Centaurs, the median perihelion of active Centaurs was smaller than that of inactive ones, and proposed a transition from amorphous to crystalline water ice to be the cause of Centaur activity. Considering only objects in our sample which satisfy the Centaur definition of Jewitt (2009), we find that Echeclus and Chiron have perihelia between those of Jupiter and Saturn, with those of our inactive Centaurs extending to beyond that of Saturn.

Table 10. Instances of nights of observation potentially indicative of cometary activity.

Object	Filter	Start Date	End Date	Cometary Activity?	Notes
Echeclus	c	2018-01-17 (MJD 58135)	2018-01-17 (MJD 58135)	Short outburst	Fan-shaped coma visible
Echeclus	o	2017-12-24 (MJD 58111)	2018-01-02 (MJD 58120)	Short outburst	Fan-shaped coma visible
Echeclus	o	2018-03-06 (MJD 58183)	2018-03-06 (MJD 58183)	Short outburst	PSF extension
Echeclus	o	2021-01-03 (MJD 59217)	2021-01-03 (MJD 59217)	No	Background stellar flux contamination
Echeclus	o	2017-11-10 (MJD 58067)	2018-02-12 (MJD 58161)	Sustained brightening	Fan-shaped coma visible
Chiron	c	2016-12-22 (MJD 57744)	2016-12-22 (MJD 57744)	No	Background stellar flux contamination
Chiron	o	2021-06-18 (MJD 59383)	2021-06-27 (MJD 59392)	Sustained brightening	No visible activity or PSF extension yet brightening beyond literature amplitude and spread of data from previous apparitions
Pluto	c	2019-07-04 (MJD 58669)	2019-07-04 (MJD 58669)	No	Background stellar flux contamination
Pluto	o	2020-10-07 (MJD 59129)	2020-10-07 (MJD 59129)	No	Background stellar flux contamination
Quaoar	o	2021-03-22 (MJD 59295)	2021-03-22 (MJD 59295)	No	Background stellar flux contamination
2014 QA43	o	2020-09-16 (MJD 59108)	2020-12-07 (MJD 59190)	Unknown	No visible coma or No PSF extension

Though our sample is too small to accurately quantify median perihelia, our observations of Centaur activity appear to be consistent with the findings of [Jewitt \(2009\)](#).

All of the variable (or comet-like activity) observations in the ATLAS dataset that correspond to instances of potential cometary activity were removed from the dataset before phase curve analyses were conducted. If any found instance of possible cometary activity was extended in time, we remove all datapoints in both filters between the start date and end date of the activity. Furthermore, any data identified by our algorithm as a bright night yet showed background star contamination were removed from the dataset. We note that the number of observations taken during an outburst remains a limiting factor in detecting such activity. For example, despite occurring during the ATLAS observation baseline, a previously-recorded outburst of Echeclus in 2016 August ([Rousselot et al. 2016](#)) did not cause a $>2\sigma$ increase in the ATLAS data, and observations were too sparse for it to be detected as lower-level cometary activity. Furthermore, any lower-level cometary activity that persisted for several consecutive apparitions would likely remain undetected, thereby reducing the accuracy of any applied phase curve fit. However, our algorithm has allowed us to detect an instance of cometary activity on Chiron despite displaying no visible coma or comet-like tail. Such activity would remain undetected from analysis of ATLAS postage stamps, yet is readily detectable in our algorithm. Therefore, we present our phase curve fits as the best analysis that can be carried out within the limits of the dataset.

6.5. HG_1G_2 Model

We apply the HG_1G_2 phase curve model to the *c* filter dataset of Hidalgo and the *o* filter phase curve of Hidalgo, Narcissus and 2014 QA43. The resulting fits to the data are shown in [Figure 23](#) and its online Figure set. [Table 12](#) lists the absolute magnitudes H and slope parameters G_1 and G_2 of these phase curves. Our best-fit slope parameters are consistent within their uncertainties with monotonic functions of positive slope, as predicted from surface reflectance models ([Muinonen et al. 2010](#); [Mahlke et al. 2021](#)). [Mahlke et al. \(2021\)](#) utilized serendipitous ATLAS observations of main belt asteroids to fit their phase curves with the HG_1G_2 function to determine possible correlations of slope parameters with main belt asteroid (MBA) taxonomic class. We aim to compare our best-fit slope parameters with those from the taxonomic classes to infer the surface types of Hidalgo, Narcissus and 2014 QA43. [Figure 24](#) displays the kernel density estimation (KDE) plots of G_1 and G_2 values of 19708 MBAs as measured by [Mahlke et al. \(2021\)](#) sorted by taxonomic complex, with our derived slope parameters for our three JFCs overplotted with their associated error bars. We include the *c* filter slope parameter of Hidalgo for completeness, but for analysis we consider only the slope parameters for our objects in the *o* filter as they were derived from more observations. As seen in [Figure 24](#), the *o* filter slope parameters of all three fitted JFCs are consistent within uncertainties with the KDE distributions of all asteroid taxonomic complexes to 3σ , with greater correspondences to the carbonaceous C-type complexes. The

60558 Echeclus

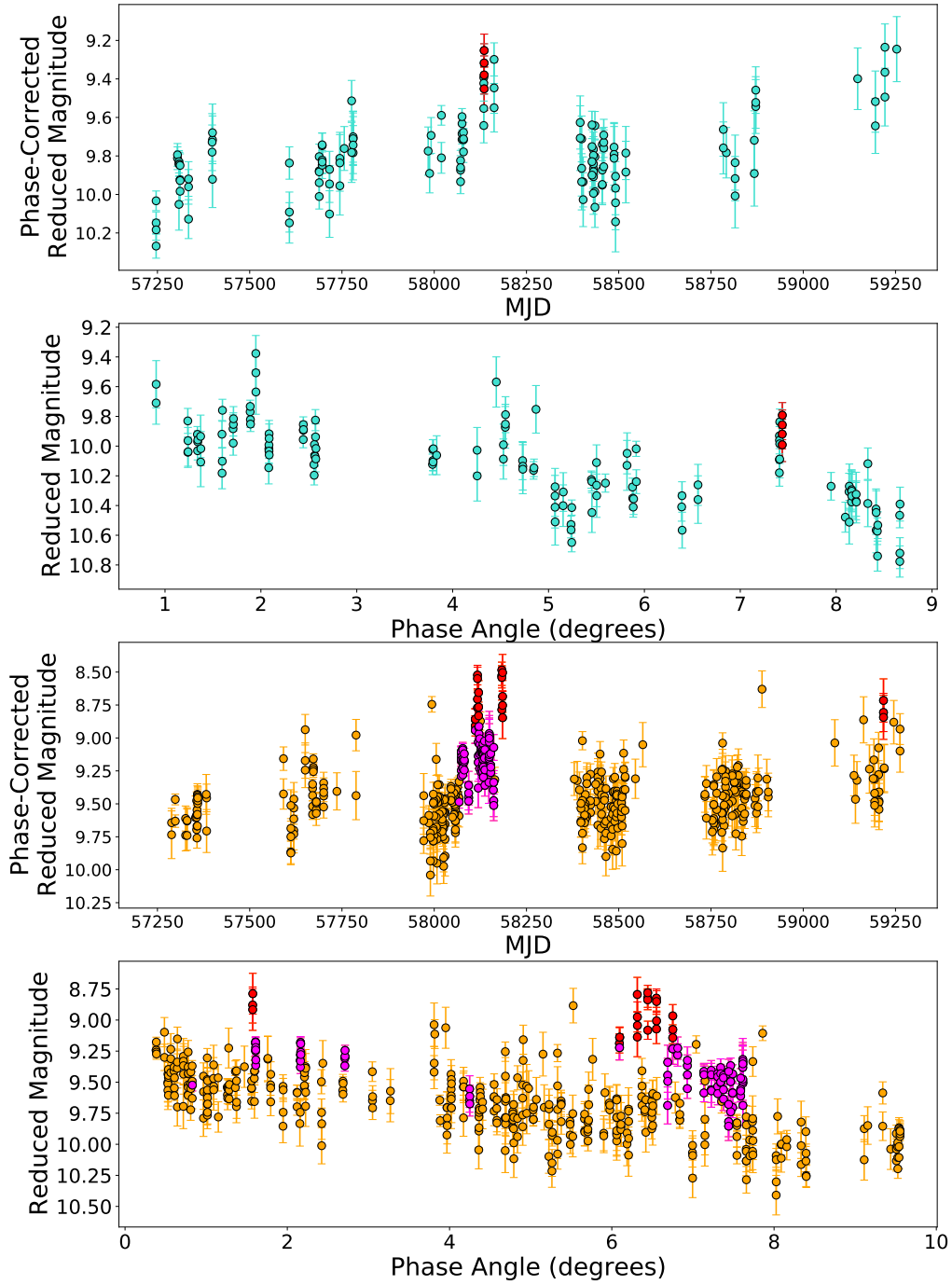


Figure 12. Plots of phase-angle corrected reduced magnitude vs. MJD in ATLAS *c* (turquoise, upper) and *o* (orange, upper) and phase curves of reduced magnitude vs. phase angle in ATLAS *c* (turquoise, lower) and *o* (orange, lower) for (60558) Echeclus. Red points denote observations taken from nights with ≥ 3 observations of which 75% are brighter than 2σ from the object's sigma-clipped median magnitude. Magenta points denote observations within a 30 day bin whose median magnitude lies 0.2 magnitudes and 1 standard deviation brighter than the object's sigma-clipped median magnitude.

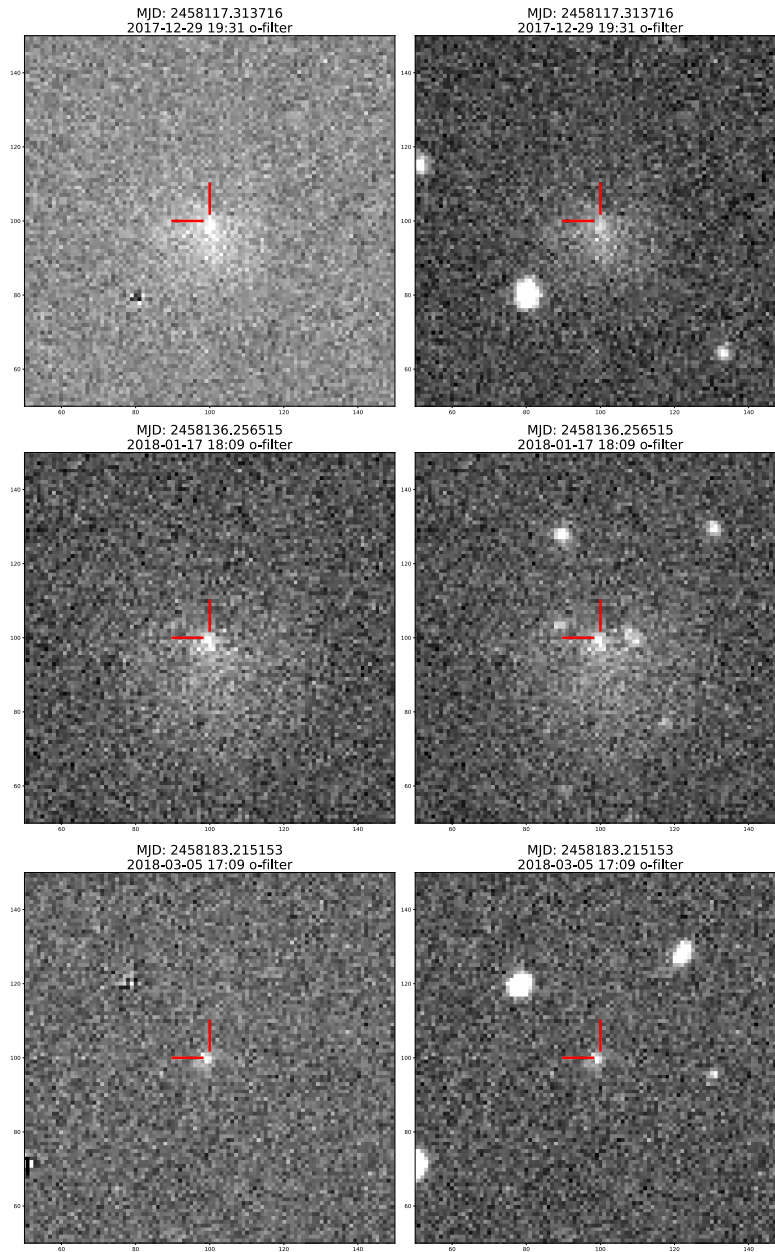


Figure 13. ATLAS difference (left) and reduced (right) images of Echeclus during its observed cometary outburst. Red crosshairs denote Echeclus’s position on the images. *Upper:* 2017 December 29 19:31 UTC (MJD 58117.313716) ATLAS *o* filter images, with fan-shaped coma clearly visible (detected from our short outburst search algorithm). *Middle:* 2018 January 17 18:09 UTC (MJD 58136.256515) ATLAS *o* filter images, with fan-shaped coma clearly visible (detected from our longer-term lower-level activity search algorithm). *Lower:* 2018 March 5 UTC 17:09 (MJD 58183.215153) ATLAS *o* filter images, showing Echeclus to appear fuzzy compared to background stars, indicating residual coma (detected from our short outburst search algorithm).

surfaces of Narcissus and 2014 QA43 remain unclassified, while Hidalgo has been previously classified as a D-type asteroid (Tholen 1984; Belskaya et al. 2017; Geem et al. 2022). Our G_1 and G_2 parameters for Hidalgo are consistent with its previous classification, lying within the 95% confidence interval, albeit just outside the core of the distribution of the D-type complex.

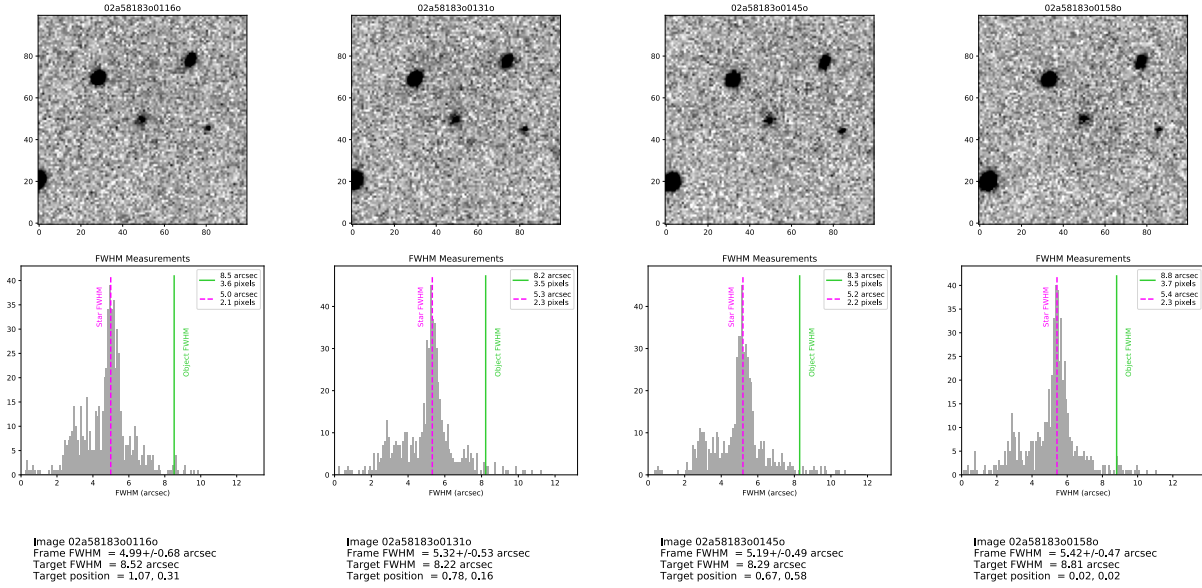


Figure 14. PSF FWHM analysis for 2018 March 6 (MJD 58183) ATLAS images of (60558) Echeclus. *Upper row:* 100x100 pixel inset of 1000x1000 pixel reduced ATLAS images centered on Echeclus. *Lower row:* Histograms of FWHM of all background stars in each 1000x1000 pixel ATLAS image, with the median stellar FWHM (dashed magenta vertical line) and Echeclus FWHM (solid green vertical line) plotted for reference. In all images, Echeclus displays significant PSF extension.

Table 11. PSF FWHM analysis for selected bright nights of Echeclus, Chiron, and 2014 QA43 compared to PSF FWHM of background stars.

Object	UTC Date and Time	MJD	PSF FWHM	
			Echeclus PSF FWHM (arcsec)	Stellar PSF FWHM (arcsec)
Echeclus	2018-03-05 17:18	58183.215153	8.52	4.99 ± 0.68
Echeclus	2018-03-05 17:20	58183.222678	8.22	5.32 ± 0.53
Echeclus	2018-03-05 17:30	58183.229396	8.29	5.19 ± 0.49
Echeclus	2018-03-05 17:39	58183.23565	8.81	5.42 ± 0.47
Chiron	2021-06-22 23:07	59388.463541	3.66	3.70 ± 0.36
Chiron	2021-06-22 23:12	59388.466769	3.79	3.61 ± 0.29
Chiron	2021-06-22 23:22	59388.474141	5.07	3.92 ± 0.33
Chiron	2021-06-22 23:48	59388.492191	4.34	3.85 ± 0.33
2014 QA43	2020-11-11 00:32	59164.522729	5.06	4.25 ± 0.19
2014 QA43	2020-11-11 01:07	59164.546531	3.86	4.02 ± 0.21
2014 QA43	2020-11-11 02:12	59164.592126	5.02	4.00 ± 0.17
2014 QA43	2020-11-11 02:23	59164.599976	3.25	4.30 ± 0.19

7. CONCLUSIONS

We use serendipitous observations from the long baseline and high cadence ATLAS survey to generate phase curves for 18 small Solar System objects, including 7 KBOs, 4 Centaurs, and 5 JFCs. We have measured the linear phase coefficients for all 18 objects in both wide-band *c* and *o* ATLAS filters. The results are as follows:

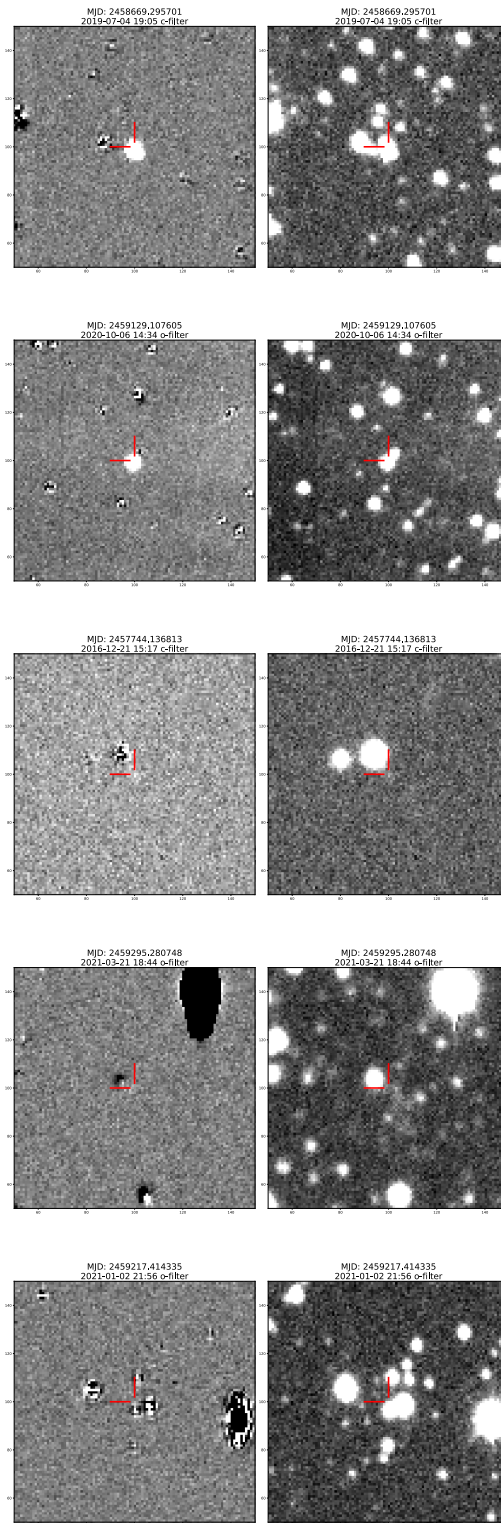


Figure 15. Collage of ATLAS difference (left) and reduced (right) images of, in descending order, Pluto (2019-07-04 19:05 UTC, *c* filter), Pluto (2020-10-06 14:34 UTC, *o* filter), Chiron (2016-12-21 15:17 UTC, *c* filter), Quaoar (2021-03-21 18:44 UTC, *o* filter), and Echeclus (2021-01-02 21:56 UTC, *o* filter). Red crosshairs denote positions of objects in images. In all images, the objects lie close to often poorly-subtracted background stars.

2060 Chiron

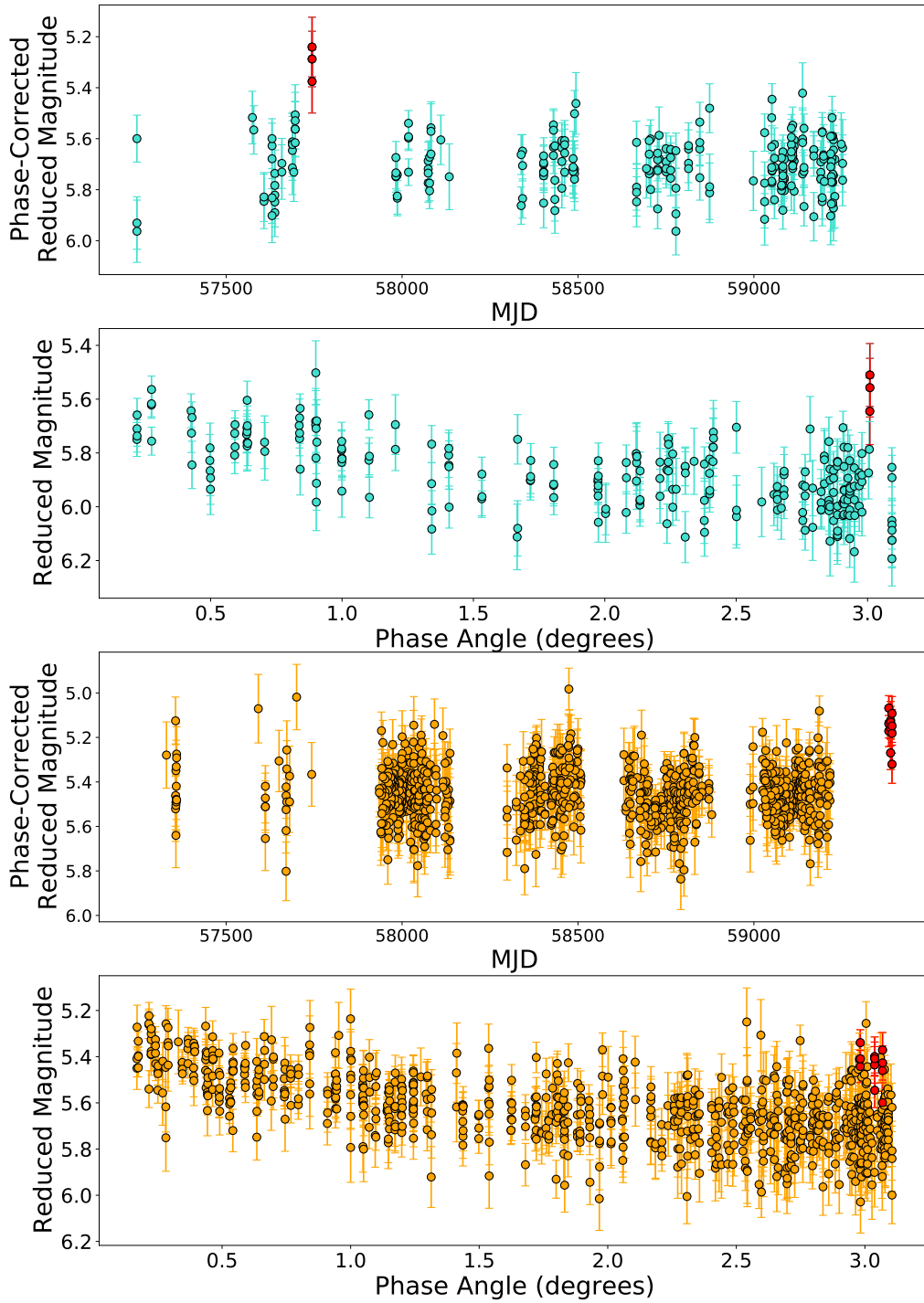


Figure 16. Plots of phase-angle corrected reduced magnitude vs. MJD in ATLAS *c* (turquoise, upper) and *o* (orange, upper) and phase curves of reduced magnitude vs. phase angle in ATLAS *c* (turquoise, lower) and *o* (orange, lower) for (2060) Chiron. Red points denote observations taken from nights with ≥ 3 observations of which 75% are brighter than 2σ from the object's median sigma-clipped magnitude.

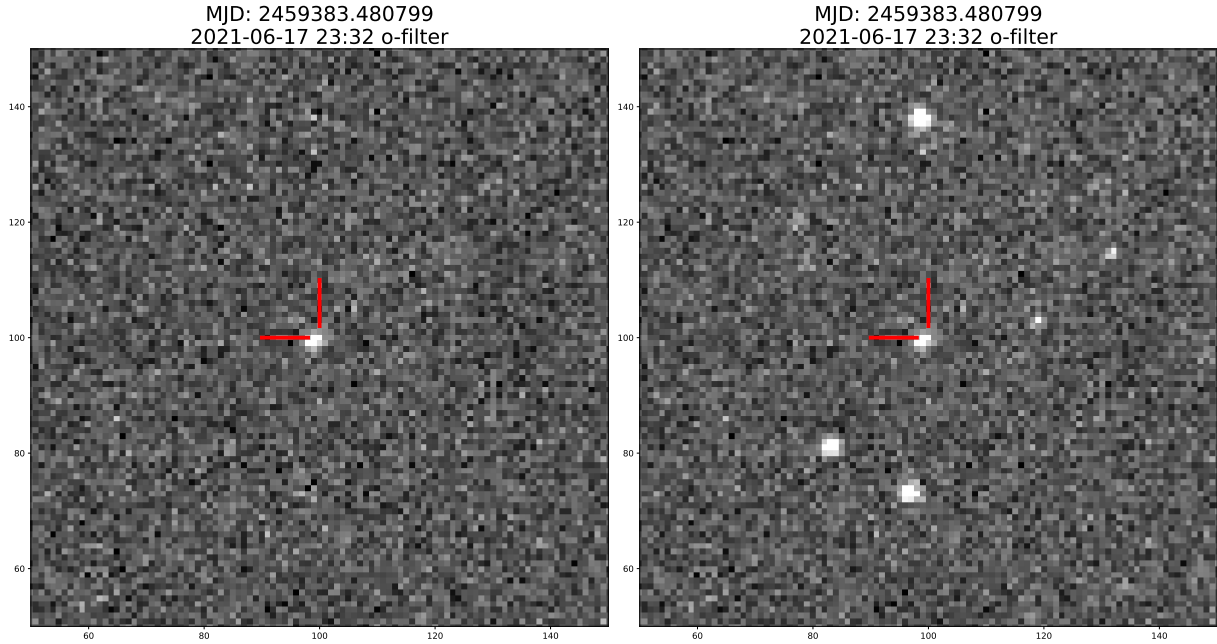


Figure 17. 2021 June 17 23:32 UTCMJD 59383.480799 ATLAS difference image (left) and reduced image (right) of Chiron during its 2021-2022 active epoch, taken in ATLAS *o* filter. Red crosshairs denote Chiron's position on the images. Chiron's signal remains point-like from visual inspection.

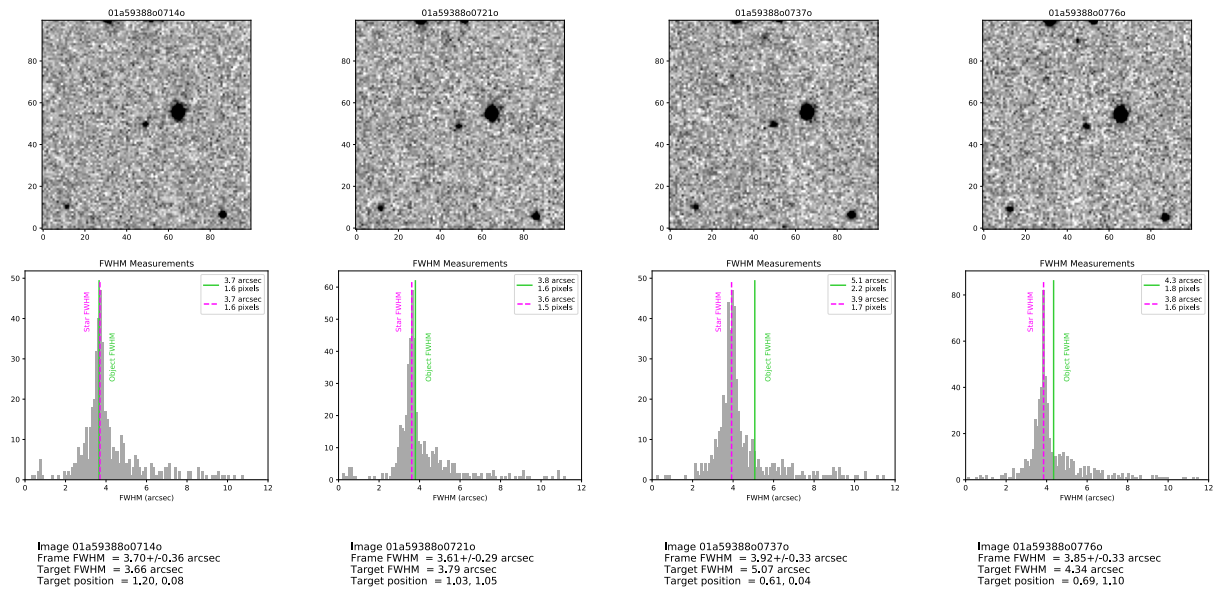


Figure 18. PSF FWHM analysis for 2021 June 23 (MJD 59388) ATLAS images of (2060) Chiron. *Upper row:* 100x100 pixel inset of 1000x1000 pixel reduced ATLAS images centered on (2060) Chiron. *Lower row:* Histograms of FWHM of all background stars in each 1000x1000 pixel ATLAS image, with the median stellar FWHM (dashed magenta vertical line) and (2060) Chiron FWHM (solid green vertical line) plotted for reference. In all images, the FWHM of (2060) Chiron remains consistent with the histogram distribution of the FWHM of background stars, with no significant extension.

134340 Pluto

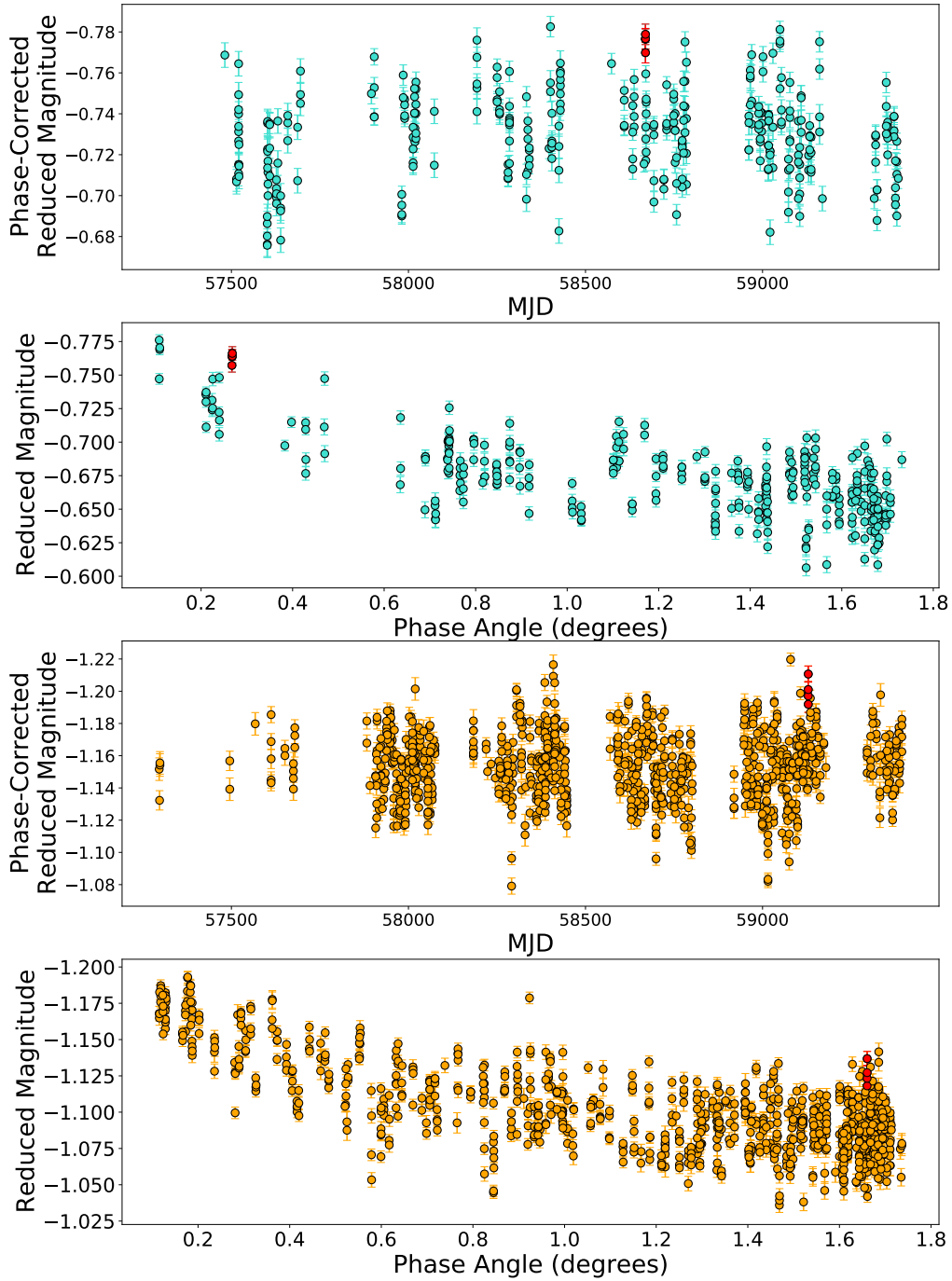


Figure 19. Plots of phase-angle corrected reduced magnitude vs. MJD in ATLAS *c* (turquoise, upper) and *o* (orange, upper) and phase curves of reduced magnitude vs. phase angle in ATLAS *c* (turquoise, lower) and *o* (orange, lower) for (134340) Pluto, also corrected for rotational modulation. Red points denote observations taken from nights with ≥ 3 observations of which 75% are brighter than 2σ from the sigma-clipped object's median magnitude.

50000 Quaoar

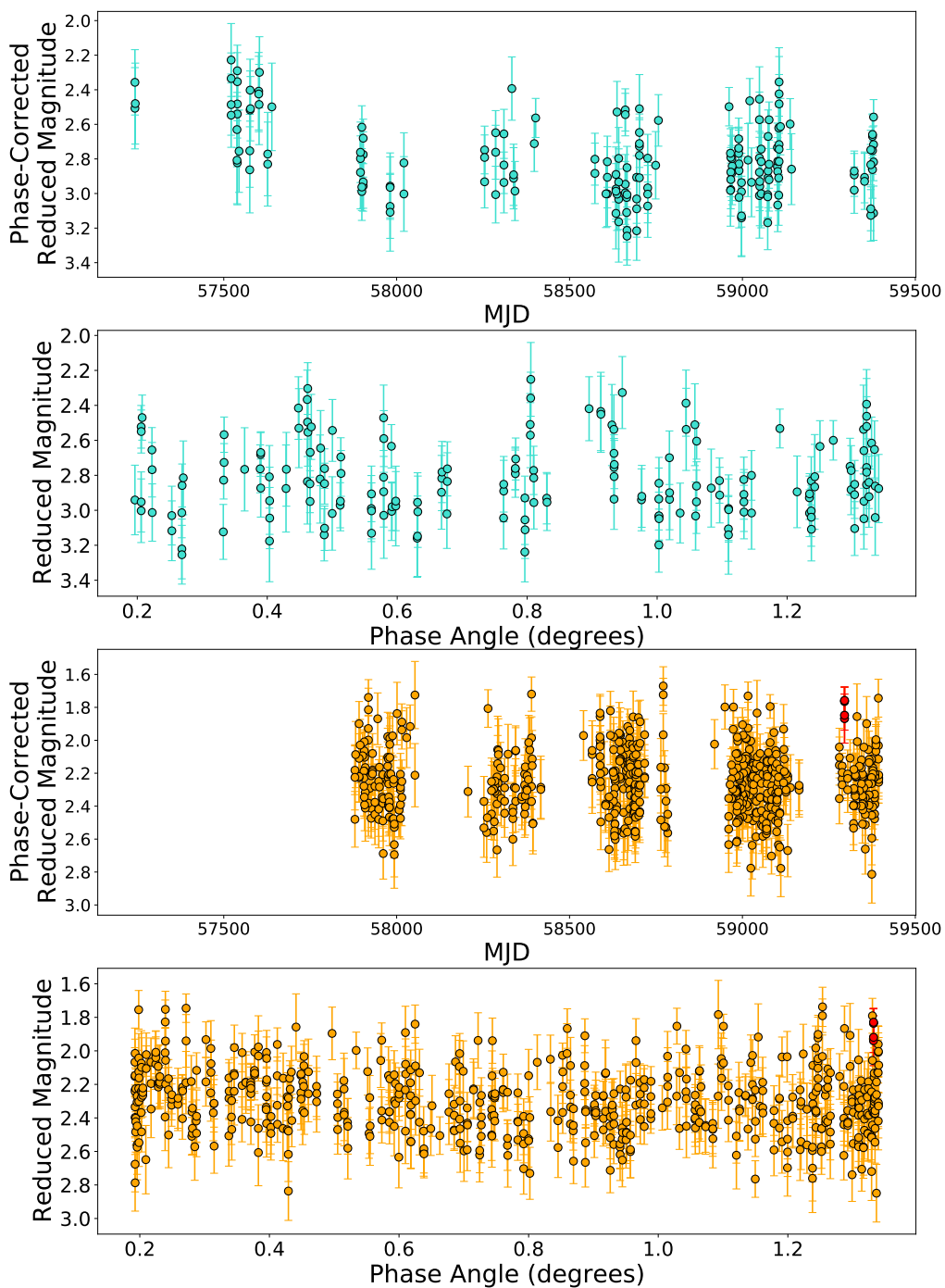


Figure 20. Plots of phase-angle corrected reduced magnitude vs. MJD in ATLAS *c* (turquoise, upper) and *o* (orange, upper) and phase curves of reduced magnitude vs. phase angle in ATLAS *c* (turquoise, lower) and *o* (orange, lower) for (50000) Quaoar, also corrected for rotational modulation. Red points denote observations taken from nights with ≥ 3 observations of which 75% are brighter than 2σ from the object's sigma-clipped median magnitude.

501585 2014 QA43

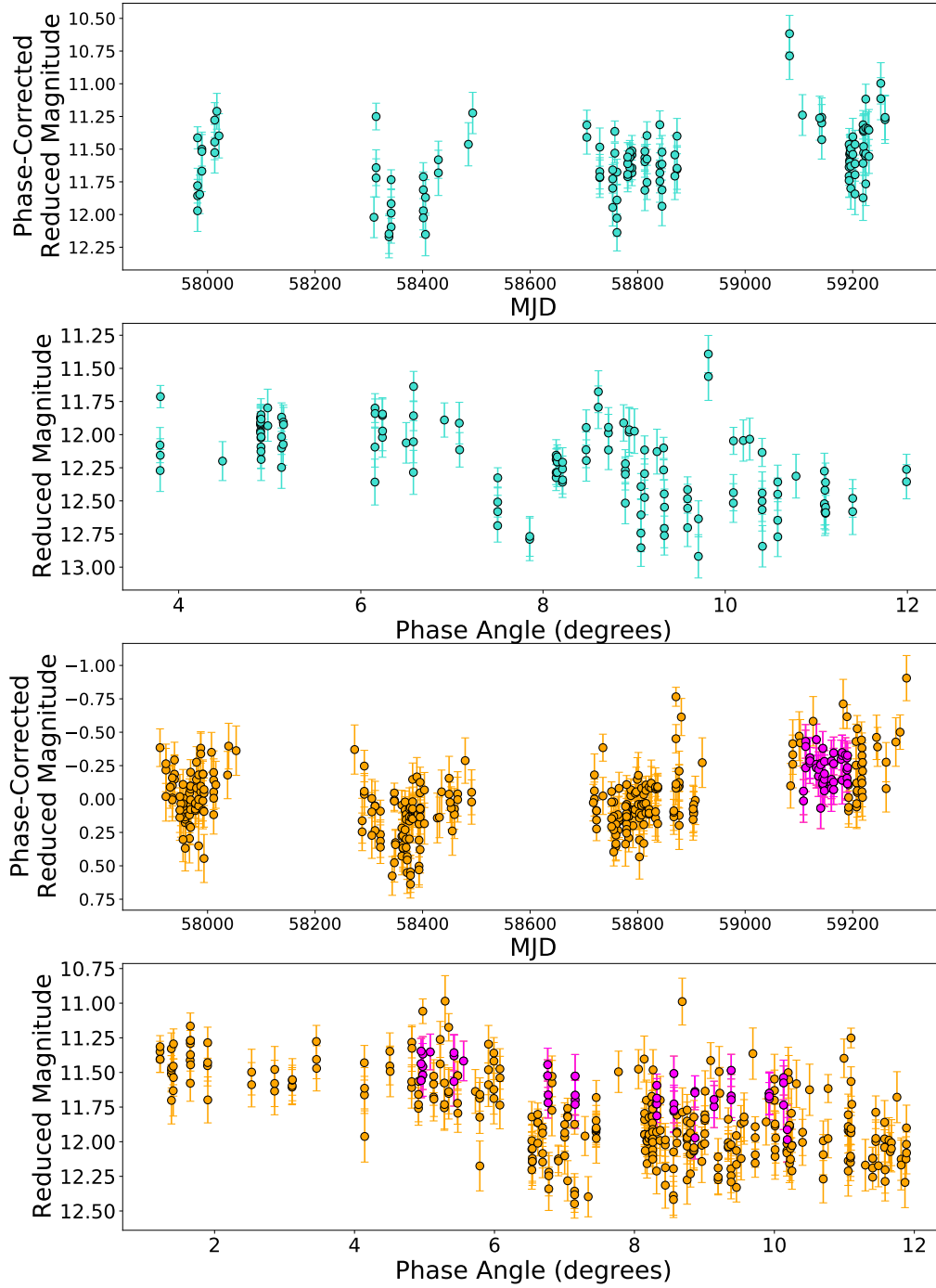


Figure 21. Plots of phase-angle corrected reduced magnitude vs. MJD in ATLAS *c* (turquoise, upper) and *o* (orange, upper) and phase curves of reduced magnitude vs. phase angle in ATLAS *c* (turquoise, lower) and *o* (orange, lower) for (501585) 2014 QA43. Red points denote observations taken from nights with ≥ 3 observations of which 75% are brighter than 2σ from the sigma-clipped object's median magnitude. Magenta points denote observations within a 30 day bin whose median magnitude lies 0.2 magnitudes and 1 standard deviation brighter than the object's sigma-clipped median magnitude.

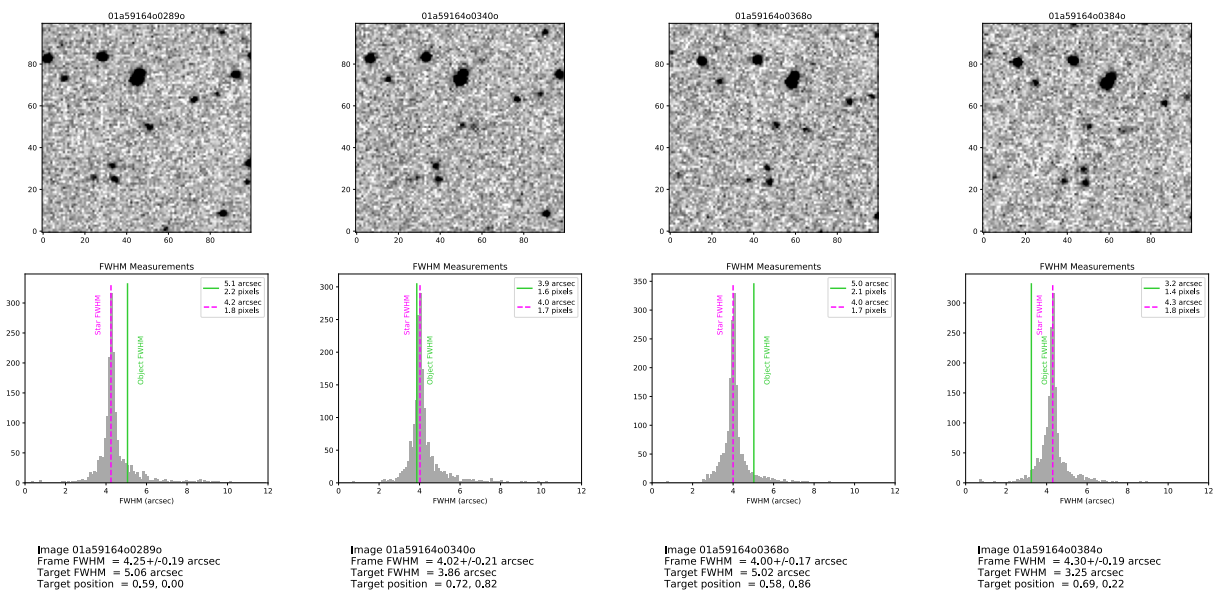


Figure 22. PSF FWHM analysis for 2020 November 11 (MJD 59164) ATLAS images of (501585) 2014 QA43. *Upper row:* 100x100 pixel inset of 1000x1000 pixel reduced ATLAS images centered on (501585) 2014 QA43. *Lower row:* Histograms of FWHM of all background stars in each 1000x1000 pixel ATLAS image, with the median stellar FWHM (dashed magenta vertical line) and (501585) 2014 QA43 FWHM (solid green vertical line) plotted for reference. The PSF of (501585) 2014 QA43 remains consistent with the histogram distribution of the FWHM of background stars, with no significant extension.

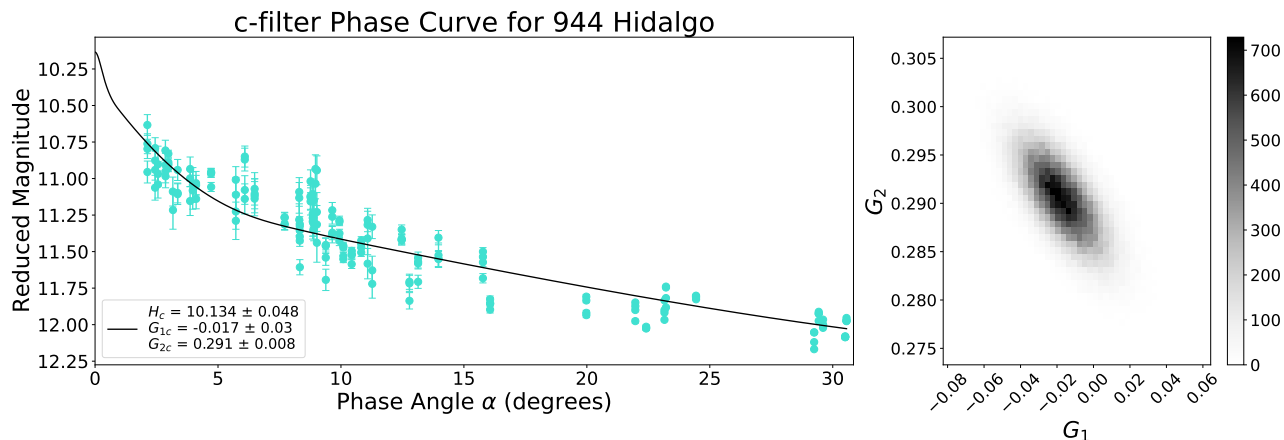


Figure 23. *Left plot:* HG_1G_2 model fit to c filter phase curve of (944) Hidalgo. *Right plot:* 2D histogram of Monte Carlo solutions to slope parameters G_1 and G_2 of HG_1G_2 fit. Best fit function extended to $\alpha = 0$ deg for ease of viewing the extrapolated absolute magnitude value and any potential opposition surge. The complete figure set (4 images) is available in the online published version of the paper.

1. Negative phase coefficients β values noted in the literature become more positive with the larger datasets from ATLAS, and are thus an artifact of small datasets with large scatter, and not a real physical phenomenon.
2. We search for correlations between phase curve parameters using phase coefficient and absolute magnitude values re-measured across the phase angle range $0.1 \leq \alpha \leq 6$ deg. We find no correlation between the linear phase coefficients and absolute magnitude for either ATLAS filter. We report no correlation between phase coefficient and color index in the o filter, and a tentative negative correlation in the c filter, consistent with the results of

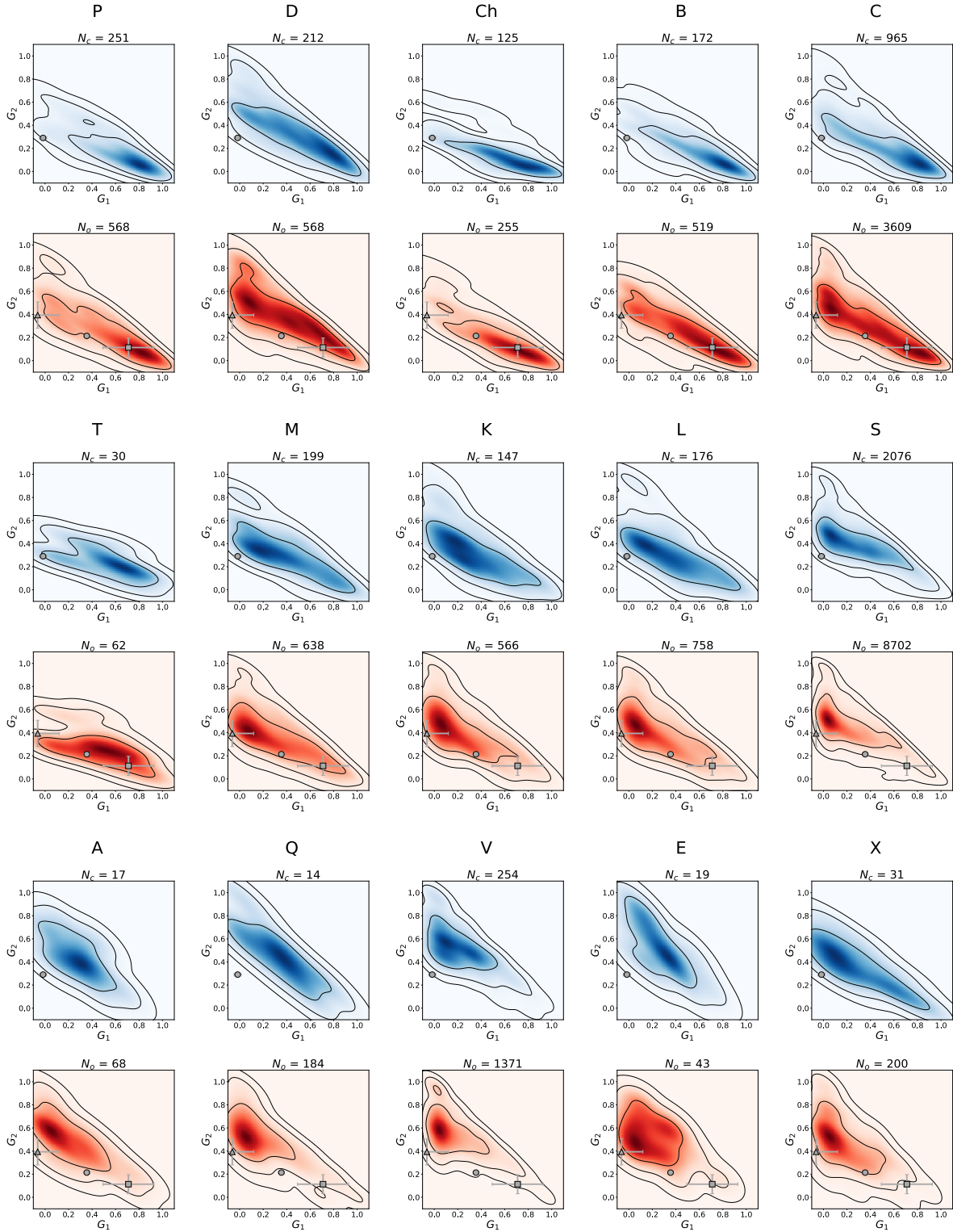


Figure 24. G_1, G_2 KDE distributions of taxonomic complexes as mapped by [Mahlke et al. \(2021\)](#) in c and o ATLAS filters, with G_1 and G_2 parameters of Hidalgo (circle), Narcissus (square), and 2014 QA43 (triangle) phase curves overplotted. Contours mark KDE levels at which 68.3% (1σ), 95% (2σ) and 99.7% (3σ) of values are encompassed. Uncertainties for Hidalgo datapoints are smaller than the plot symbol.

Table 12. H , G_1 , and G_2 parameters, their associated 2σ uncertainties, and the number of datapoints N for objects that satisfy criteria for fitting with the HG_1G_2 model.

Object	H	G_1	G_2	N
Hidalgo (<i>c</i> filter)	10.135 ± 0.048	-0.017 ± 0.03	0.291 ± 0.008	178
Hidalgo (<i>o</i> filter)	10.193 ± 0.026	0.355 ± 0.024	0.214 ± 0.006	730
Narcissus (<i>o</i> filter)	13.044 ± 0.124	0.71 ± 0.216	0.113 ± 0.083	204
2014 QA43 (<i>o</i> filter)	10.899 ± 0.093	-0.063 ± 0.178	0.393 ± 0.106	270

Ayala-Loera et al. (2018) and Alvarez-Candal et al. (2019). We find a tentative negative correlation between relative phase coefficient and object color index in the ATLAS *c* and *o* filters, consistent with the findings of Ayala-Loera et al. (2018) and Alvarez-Candal et al. (2019), though an increase in sample size would help to better resolve this correlation.

3. Splitting our sample into sub-populations, no significant correlation is found between phase coefficient and absolute magnitude in either filter. Tentative correlations are found in the ATLAS *c* filter between phase coefficient and color index for all sub-populations, and in the *o* filter for the Centaur/JFCs/Transition Objects and non-dwarf planet sub-populations. We find a tentative negative correlation between relative phase coefficient and object surface color for the KBO population, the dwarf planet population, and all non-dwarf planet objects, consistent with the results of Ayala-Loera et al. (2018) and Alvarez-Candal et al. (2019). The apparent lack of correlation exhibited by the Centaurs/JFCs/Transition Objects compared to the KBOs may indicate a difference in surface properties, but a larger sample size is needed to confirm this.
4. We detect comet-like activity exhibited by Echeclus (corresponding to previous literature outbursts) and Chiron (corresponding to a newly discovered epoch of activity reported by Dobson et al. (2021b)), and we also detect potential cometary activity for 2014 QA43. This complements established methods looking for extended PSFs and faint coma or tails in images to detect epochs of cometary activity.
5. We apply the HG_1G_2 model to the phase curves of 3 JFCs - Hidalgo, Narcissus, and 2014 QA43. We find their best-fitting slope parameters to be more consistent with carbonaceous main belt asteroid taxonomic complexes than siliceous ones, indicating low-albedo, carbon-rich surfaces for these objects.

The long baseline and high observation cadence of ATLAS has yielded larger photometric datasets per object in our sample than any previous study. Future surveys utilising larger telescope diameters, such as the Rubin Observatory Legacy Survey of Space and Time (LSST) by the Vera C. Rubin Observatory (LSST Science Collaboration et al. 2009; Jurić et al. 2019; Ivezić et al. 2019), though operating with a lower observation cadence than ATLAS, will help reduce uncertainties in magnitude measurements, aiding discovery of and correction for rotational lightcurves. LSST will also significantly increase the number of objects whose phase curves can be analysed by probing to fainter limiting magnitudes, allowing increased accuracy for characterizing larger numbers of the KBO, Centaur, and JFC populations.

8. ACKNOWLEDGEMENTS

This work has made use of data from the Asteroid Terrestrial- impact Last Alert System (ATLAS) project. The Asteroid Terrestrial- impact Last Alert System (ATLAS) project is primarily funded to search for near earth asteroids through NASA grants NN12AR55G, 80NSSC18K0284, and 80NSSC18K1575; byproducts of the NEO search include images and catalogs from the survey area. The ATLAS science products have been made possible through the contributions of the University of Hawaii Institute for Astronomy, the Queen’s University Belfast, the Space Telescope Science Institute, the South African Astronomical Observatory, and the Millennium Institute of Astrophysics (MAS), Chile. MES and MMD were supported by the UK Science Technology Facilities Council (STFC) grants ST/V000691/1 and ST/V506990/1, respectively. LJS acknowledges support by the European Research Council (ERC) under the European Union’s Horizon 2020 research and innovation program (ERC Advanced Grant KILONOVA No. 885281).

This research has made use of data and services provided by the Horizons system of the Jet Propulsion Laboratory, and has made use of services provided by NASA’s Astrophysics Data System. All photometric data used in this study is available from the online ATLAS Forced Photometry Server at <https://fallingstar-data.com/forcedphot/>.

The authors thank the researchers Grigori Fedorets, David Jackson, Lucy Dolan, and Will Bate for useful feedback on the manuscript. The authors thank the entire ATLAS Collaboration for their productive discussion on this paper. The authors thank the anonymous reviewers for their feedback that improved the manuscript of this paper.

Facilities: ATLAS (Maunaloa and Haleakalā telescopes)

Software: Astropy (Astropy Collaboration et al. 2013, 2018), Jupyter Notebook (Kluyver et al. 2016), lmfit (Newville et al. 2014), math (Van Rossum 2020), Matplotlib (Hunter 2007), Numpy (van der Walt et al. 2011; Harris et al. 2020), os (Van Rossum 2020), Pandas (pandas development team 2020), python (<https://www.python.org>), SAOImageDS9 (Joye 2019), sbpy (Mommert et al. 2019), SciPy (Virtanen et al. 2020), seaborn (Waskom 2021)

REFERENCES

- Alvarez-Candal, A., Ayala-Loera, C., Gil-Hutton, R., et al. 2019, MNRAS, 488, 3035, doi: [10.1093/mnras/stz1880](https://doi.org/10.1093/mnras/stz1880)
- Alvarez-Candal, A., Jimenez Corral, S., & Colazo, M. 2022, A&A, 667, A81, doi: [10.1051/0004-6361/202243479](https://doi.org/10.1051/0004-6361/202243479)
- Alvarez-Candal, A., Pinilla-Alonso, N., Ortiz, J. L., et al. 2016, A&A, 586, A155, doi: [10.1051/0004-6361/201527161](https://doi.org/10.1051/0004-6361/201527161)
- Astropy Collaboration, Robitaille, T. P., Tollerud, E. J., et al. 2013, A&A, 558, A33, doi: [10.1051/0004-6361/201322068](https://doi.org/10.1051/0004-6361/201322068)
- Astropy Collaboration, Price-Whelan, A. M., Sipőcz, B. M., et al. 2018, AJ, 156, 123, doi: [10.3847/1538-3881/aabc4f](https://doi.org/10.3847/1538-3881/aabc4f)
- Ayala-Loera, C., Alvarez-Candal, A., Ortiz, J. L., et al. 2018, MNRAS, 481, 1848, doi: [10.1093/mnras/sty2363](https://doi.org/10.1093/mnras/sty2363)
- Bagnulo, S., Boehnhardt, H., Muinonen, K., et al. 2006, A&A, 450, 1239, doi: [10.1051/0004-6361:20054518](https://doi.org/10.1051/0004-6361:20054518)
- Baluev, R. V. 2008, MNRAS, 385, 1279, doi: [10.1111/j.1365-2966.2008.12689.x](https://doi.org/10.1111/j.1365-2966.2008.12689.x)
- Bauer, J. M., Grav, T., Mainzer, A. K., et al. 2013, in AAS/Division for Planetary Sciences Meeting Abstracts, Vol. 45, AAS/Division for Planetary Sciences Meeting Abstracts #45, 508.06
- Belskaya, I. N., Levasseur-Regourd, A. C., Shkuratov, Y. G., & Muinonen, K. 2008, Surface Properties of Kuiper Belt Objects and Centaurs from Photometry and Polarimetry, ed. M. A. Barucci, H. Boehnhardt, D. P. Cruikshank, A. Morbidelli, & R. Dotson, 115
- Belskaya, I. N., Fornasier, S., Tozzi, G. P., et al. 2017, Icarus, 284, 30, doi: [10.1016/j.icarus.2016.11.003](https://doi.org/10.1016/j.icarus.2016.11.003)
- Benecci, S. D., Lisse, C. M., Ryan, E. L., et al. 2018, Icarus, 314, 265, doi: [10.1016/j.icarus.2018.05.015](https://doi.org/10.1016/j.icarus.2018.05.015)
- Bernstein, G. M., Trilling, D. E., Allen, R. L., et al. 2004, AJ, 128, 1364, doi: [10.1086/422919](https://doi.org/10.1086/422919)
- Binzel, R. P., & Mulholland, J. D. 1984, AJ, 89, 1759, doi: [10.1086/113685](https://doi.org/10.1086/113685)
- Bowell, E., Hapke, B., Domingue, D., et al. 1989, in Asteroids II, ed. R. P. Binzel, T. Gehrels, & M. S. Matthews, 524–556
- Brown, M. E. 2008, The Largest Kuiper Belt Objects, ed. M. A. Barucci, H. Boehnhardt, D. P. Cruikshank, A. Morbidelli, & R. Dotson, 335
- . 2012, Annual Review of Earth and Planetary Sciences, 40, 467, doi: [10.1146/annurev-earth-042711-105352](https://doi.org/10.1146/annurev-earth-042711-105352)
- Brown, M. E., Schaller, E. L., & Fraser, W. C. 2011, ApJL, 739, L60, doi: [10.1088/2041-8205/739/2/L60](https://doi.org/10.1088/2041-8205/739/2/L60)

- Brown, M. E., Trujillo, C. A., & Rabinowitz, D. L. 2005, *ApJL*, 635, L97, doi: [10.1086/499336](https://doi.org/10.1086/499336)
- Buie, M. W., Grundy, W. M., Young, E. F., Young, L. A., & Stern, S. A. 2010, *AJ*, 139, 1117, doi: [10.1088/0004-6256/139/3/1117](https://doi.org/10.1088/0004-6256/139/3/1117)
- Buie, M. W., Tholen, D. J., & Wasserman, L. H. 1997, *Icarus*, 125, 233, doi: [10.1006/icar.1996.5624](https://doi.org/10.1006/icar.1996.5624)
- Buratti, B. J., Hillier, J. K., Heinze, A., et al. 2003, *Icarus*, 162, 171, doi: [10.1016/S0019-1035\(02\)00068-4](https://doi.org/10.1016/S0019-1035(02)00068-4)
- Bus, S. J., Bowell, E., & French, L. M. 1988, *IAUC*, 4684, 2
- Carusi, A., & Valsecchi, G. B. 1987, *Publications of the Astronomical Institute of the Czechoslovak Academy of Sciences*, 2, 21
- Chandler, C. O., Kueny, J. K., Trujillo, C. A., Trilling, D. E., & Oldroyd, W. J. 2020, *ApJL*, 892, L38, doi: [10.3847/2041-8213/ab7dc6](https://doi.org/10.3847/2041-8213/ab7dc6)
- Choi, Y. J., Weissman, P., Chesley, S., et al. 2006a, *Central Bureau Electronic Telegrams*, 563, 1
- Choi, Y. J., Weissman, P. R., & Polishook, D. 2006b, *IAUC*, 8656, 2
- Cruikshank, D. P., & Dalle Ore, C. M. 2003, *Earth Moon and Planets*, 92, 315, doi: [10.1023/B:MOON.0000031948.39136.7d](https://doi.org/10.1023/B:MOON.0000031948.39136.7d)
- Dahlgren, M., Lagerkvist, C. I., Fitzsimmons, A., & Williams, I. P. 1991, *MNRAS*, 250, 115, doi: [10.1093/mnras/250.1.115](https://doi.org/10.1093/mnras/250.1.115)
- Delsanti, A., & Jewitt, D. 2006, *The Solar System Beyond The Planets*, ed. P. Blondel & J. W. Mason, 267, doi: [10.1007/3-540-37683-6_11](https://doi.org/10.1007/3-540-37683-6_11)
- Delsanti, A., Merlin, F., Guilbert-Lepoutre, A., et al. 2010, *A&A*, 520, A40, doi: [10.1051/0004-6361/201014296](https://doi.org/10.1051/0004-6361/201014296)
- Dobson, M., Fitzsimmons, A., Schwamb, M. E., et al. 2021a, *The Astronomer's Telegram*, 14903, 1
- Dobson, M. M., Schwamb, M. E., Fitzsimmons, A., et al. 2021b, *Research Notes of the American Astronomical Society*, 5, 211, doi: [10.3847/2515-5172/ac26c9](https://doi.org/10.3847/2515-5172/ac26c9)
- Duffard, R., Lazzaro, D., Pinto, S., et al. 2002, *Icarus*, 160, 44, doi: [10.1006/icar.2002.6938](https://doi.org/10.1006/icar.2002.6938)
- Duncan, M. J., & Levison, H. F. 1997, *Science*, 276, 1670, doi: [10.1126/science.276.5319.1670](https://doi.org/10.1126/science.276.5319.1670)
- Elliot, J. L., Olkin, C. B., Dunham, E. W., et al. 1995, *Nature*, 373, 46, doi: [10.1038/373046a0](https://doi.org/10.1038/373046a0)
- Erasmus, N., Navarro-Meza, S., McNeill, A., et al. 2020, *ApJS*, 247, 13, doi: [10.3847/1538-4365/ab5e88](https://doi.org/10.3847/1538-4365/ab5e88)
- Fernández-Valenzuela, E., Ortiz, J. L., Duffard, R., Morales, N., & Santos-Sanz, P. 2017, *MNRAS*, 466, 4147, doi: [10.1093/mnras/stw3264](https://doi.org/10.1093/mnras/stw3264)
- Fernández, Y., Kelley, M., Lamy, P., et al. 2013, *Icarus*, 226, 1138, doi: <https://doi.org/10.1016/j.icarus.2013.07.021>
- Fornasier, S., Lazzaro, D., Alvarez-Candal, A., et al. 2014, *A&A*, 568, L11, doi: [10.1051/0004-6361/201424439](https://doi.org/10.1051/0004-6361/201424439)
- Fraser, W. C., & Brown, M. E. 2010, *ApJ*, 714, 1547, doi: [10.1088/0004-637X/714/2/1547](https://doi.org/10.1088/0004-637X/714/2/1547)
- Galiazzo, M., de la Fuente Marcos, C., de la Fuente Marcos, R., et al. 2016, *Ap&SS*, 361, 212, doi: [10.1007/s10509-016-2801-5](https://doi.org/10.1007/s10509-016-2801-5)
- Geem, J., Ishiguro, M., Bach, Y. P., et al. 2022, *A&A*, 658, A158, doi: [10.1051/0004-6361/202142014](https://doi.org/10.1051/0004-6361/202142014)
- Gladman, B., Marsden, B. G., & Vanlaerhoven, C. 2008, *Nomenclature in the Outer Solar System*, ed. M. A. Barucci, H. Boehnhardt, D. P. Cruikshank, A. Morbidelli, & R. Dotson, 43
- Hanuš, J., Ďurech, J., Oszkiewicz, D. A., et al. 2016, *A&A*, 586, A108, doi: [10.1051/0004-6361/201527441](https://doi.org/10.1051/0004-6361/201527441)
- Hapke, B. 1963, *AJ*, 68, 279, doi: [10.1086/108962](https://doi.org/10.1086/108962)
- . 1966, *AJ*, 71, 386, doi: [10.1086/110149](https://doi.org/10.1086/110149)
- . 1968, *Science*, 159, 76, doi: [10.1126/science.159.3810.76](https://doi.org/10.1126/science.159.3810.76)
- . 1981, *J. Geophys. Res.*, 86, 3039, doi: [10.1029/JB086iB04p03039](https://doi.org/10.1029/JB086iB04p03039)
- . 1984, *Icarus*, 59, 41, doi: [10.1016/0019-1035\(84\)90054-X](https://doi.org/10.1016/0019-1035(84)90054-X)
- . 1986, *Icarus*, 67, 264, doi: [10.1016/0019-1035\(86\)90108-9](https://doi.org/10.1016/0019-1035(86)90108-9)
- . 2002, *Icarus*, 157, 523, doi: [10.1006/icar.2002.6853](https://doi.org/10.1006/icar.2002.6853)
- . 2008, *Icarus*, 195, 918, doi: [10.1016/j.icarus.2008.01.003](https://doi.org/10.1016/j.icarus.2008.01.003)
- . 2012, *Icarus*, 221, 1079, doi: [10.1016/j.icarus.2012.10.022](https://doi.org/10.1016/j.icarus.2012.10.022)
- . 2021, *Icarus*, 354, 114105, doi: [10.1016/j.icarus.2020.114105](https://doi.org/10.1016/j.icarus.2020.114105)
- Harris, C. R., Millman, K. J., van der Walt, S. J., et al. 2020, *Nature*, 585, 357, doi: [10.1038/s41586-020-2649-2](https://doi.org/10.1038/s41586-020-2649-2)
- Heinze, A. N., & de Lahunta, D. 2009, *AJ*, 138, 428, doi: [10.1088/0004-6256/138/2/428](https://doi.org/10.1088/0004-6256/138/2/428)
- Hromakina, T. A., Belskaya, I. N., Krugly, Y. N., et al. 2019, *A&A*, 625, A46, doi: [10.1051/0004-6361/201935274](https://doi.org/10.1051/0004-6361/201935274)
- Hunter, J. D. 2007, *Computing in Science & Engineering*, 9, 90, doi: [10.1109/MCSE.2007.55](https://doi.org/10.1109/MCSE.2007.55)
- Ivezić, Ž., Kahn, S. M., Tyson, J. A., et al. 2019, *ApJ*, 873, 111, doi: [10.3847/1538-4357/ab042c](https://doi.org/10.3847/1538-4357/ab042c)
- Jaeger, M., Prosperi, E., Vollmann, W., et al. 2011, *IAUC*, 9213, 2
- James, N. D. 2018, *Journal of the British Astronomical Association*, 128, 51
- Jewitt, D. 2009, *AJ*, 137, 4296, doi: [10.1088/0004-6256/137/5/4296](https://doi.org/10.1088/0004-6256/137/5/4296)
- Joye, W. 2019, *SAOImageDS9/SAOImageDS9 v8.0.1*, v8.0.1, Zenodo, Zenodo, doi: [10.5281/zenodo.2530958](https://doi.org/10.5281/zenodo.2530958)
- Jurić, M., Jones, R. L., Bryce Kalmbach, J., et al. 2019, *arXiv e-prints*, arXiv:1901.08549, <https://arxiv.org/abs/1901.08549>

- Kareta, T., Sharkey, B., Noonan, J., et al. 2019, *AJ*, 158, 255, doi: [10.3847/1538-3881/ab505f](https://doi.org/10.3847/1538-3881/ab505f)
- Kavelaars, J., Jones, L., Gladman, B., Parker, J. W., & Petit, J. M. 2008, *The Orbital and Spatial Distribution of the Kuiper Belt*, ed. M. A. Barucci, H. Boehnhardt, D. P. Cruikshank, A. Morbidelli, & R. Dotson, 59
- Kluyver, T., Ragan-Kelley, B., Pérez, F., et al. 2016, in *Positioning and Power in Academic Publishing: Players, Agents and Agendas*, ed. F. Loizides & B. Schmidt (IOS Press), 87–90. <https://eprints.soton.ac.uk/403913/>
- Kokotanekova, R., Snodgrass, C., Lacerda, P., et al. 2018, *MNRAS*, 479, 4665, doi: [10.1093/mnras/sty1529](https://doi.org/10.1093/mnras/sty1529)
- . 2017, *MNRAS*, 471, 2974, doi: [10.1093/mnras/stx1716](https://doi.org/10.1093/mnras/stx1716)
- Lacerda, P., Jewitt, D., & Peixinho, N. 2008, *AJ*, 135, 1749, doi: [10.1088/0004-6256/135/5/1749](https://doi.org/10.1088/0004-6256/135/5/1749)
- Lazzaro, D., Florczak, M. A., Angeli, C. A., et al. 1997a, *Planet. Space Sci.*, 45, 1607, doi: [10.1016/S0032-0633\(97\)00124-4](https://doi.org/10.1016/S0032-0633(97)00124-4)
- . 1997b, *Planet. Space Sci.*, 45, 1607, doi: [10.1016/S0032-0633\(97\)00124-4](https://doi.org/10.1016/S0032-0633(97)00124-4)
- Leiva, R., Sicardy, B., Camargo, J. I. B., et al. 2017, *AJ*, 154, 159, doi: [10.3847/1538-3881/aa8956](https://doi.org/10.3847/1538-3881/aa8956)
- Lellouch, E., Kiss, C., Santos-Sanz, P., et al. 2010, *A&A*, 518, L147, doi: [10.1051/0004-6361/201014648](https://doi.org/10.1051/0004-6361/201014648)
- Levison, H. F. 1996, in *Astronomical Society of the Pacific Conference Series*, Vol. 107, *Completing the Inventory of the Solar System*, ed. T. Rettig & J. M. Hahn, 173–191
- Levison, H. F., & Duncan, M. J. 1994, *Icarus*, 108, 18, doi: [10.1006/icar.1994.1039](https://doi.org/10.1006/icar.1994.1039)
- . 1997, *Icarus*, 127, 13, doi: [10.1006/icar.1996.5637](https://doi.org/10.1006/icar.1996.5637)
- Li, J. Y., Helfenstein, P., Buratti, B., Takir, D., & Clark, B. E. 2015, in *Asteroids IV*, 129–150, doi: [10.2458/azu_uapress.9780816532131-ch007](https://doi.org/10.2458/azu_uapress.9780816532131-ch007)
- Licandro, J., Pinilla-Alonso, N., Pedani, M., et al. 2006, *A&A*, 445, L35, doi: [10.1051/0004-6361:200500219](https://doi.org/10.1051/0004-6361:200500219)
- Lilly, E., Hsieh, H., Bauer, J., et al. 2021, *PSJ*, 2, 155, doi: [10.3847/PSJ/ac139e](https://doi.org/10.3847/PSJ/ac139e)
- Lockwood, A. C., Brown, M. E., & Stansberry, J. 2014, *Earth Moon and Planets*, 111, 127, doi: [10.1007/s11038-014-9430-1](https://doi.org/10.1007/s11038-014-9430-1)
- Lomb, N. R. 1976, *Ap&SS*, 39, 447, doi: [10.1007/BF00648343](https://doi.org/10.1007/BF00648343)
- Lowry, S., Fitzsimmons, A., Lamy, P., & Weissman, P. 2008, in *The Solar System Beyond Neptune*, ed. M. A. Barucci, H. Boehnhardt, D. P. Cruikshank, A. Morbidelli, & R. Dotson, 397
- LSST Science Collaboration, Abell, P. A., Allison, J., et al. 2009, arXiv e-prints, arXiv:0912.0201. <https://arxiv.org/abs/0912.0201>
- Luu, J. X., & Jewitt, D. C. 1990, *AJ*, 100, 913, doi: [10.1086/115571](https://doi.org/10.1086/115571)
- Mahlke, M., Carry, B., & Denneau, L. 2021, *Icarus*, 354, 114094, doi: [10.1016/j.icarus.2020.114094](https://doi.org/10.1016/j.icarus.2020.114094)
- Marcialis, R. L., & Buratti, B. J. 1993, *Icarus*, 104, 234, doi: [10.1006/icar.1993.1098](https://doi.org/10.1006/icar.1993.1098)
- McNeill, A., Erasmus, N., Trilling, D. E., et al. 2021, *PSJ*, 2, 6, doi: [10.3847/PSJ/abcccd](https://doi.org/10.3847/PSJ/abcccd)
- Mommert, M., Kelley, M., de Val-Borro, M., et al. 2019, *The Journal of Open Source Software*, 4, 1426, doi: [10.21105/joss.01426](https://doi.org/10.21105/joss.01426)
- Muinsonen, K., Belskaya, I. N., Cellino, A., et al. 2010, *Icarus*, 209, 542, doi: [10.1016/j.icarus.2010.04.003](https://doi.org/10.1016/j.icarus.2010.04.003)
- Nelson, R. M., Hapke, B. W., Smythe, W. D., & Spilker, L. J. 2000, *Icarus*, 147, 545, doi: [10.1006/icar.2000.6454](https://doi.org/10.1006/icar.2000.6454)
- Newville, M., Stensitzki, T., Allen, D. B., & Ingargiola, A. 2014, *LMFIT: Non-Linear Least-Square Minimization and Curve-Fitting for Python, 0.8.0*, Zenodo, Zenodo, doi: [10.5281/zenodo.11813](https://doi.org/10.5281/zenodo.11813)
- Ortiz, J. L., Baumont, S., Gutiérrez, P. J., & Roos-Serote, M. 2002, *A&A*, 388, 661, doi: [10.1051/0004-6361:20020487](https://doi.org/10.1051/0004-6361:20020487)
- Ortiz, J. L., Gutiérrez, P. J., Sota, A., Casanova, V., & Teixeira, V. R. 2003, *A&A*, 409, L13, doi: [10.1051/0004-6361:20031253](https://doi.org/10.1051/0004-6361:20031253)
- Ortiz, J. L., Cikota, A., Cikota, S., et al. 2011, *A&A*, 525, A31, doi: [10.1051/0004-6361/201015309](https://doi.org/10.1051/0004-6361/201015309)
- pandas development team, T. 2020, *pandas-dev/pandas: Pandas, latest*, Zenodo, doi: [10.5281/zenodo.3509134](https://doi.org/10.5281/zenodo.3509134)
- Peixinho, N., Thirouin, A., Tegler, S. C., et al. 2020, *From Centaurs to Comets - 40 years*, ed. D. Prialnik, M. A. Barucci, & L. Young, 307–329, doi: [10.1016/B978-0-12-816490-7.00014-X](https://doi.org/10.1016/B978-0-12-816490-7.00014-X)
- Penttilä, A., Shevchenko, V. G., Wilkman, O., & Muinsonen, K. 2016, *Planet. Space Sci.*, 123, 117, doi: [10.1016/j.pss.2015.08.010](https://doi.org/10.1016/j.pss.2015.08.010)
- Rabinowitz, D. L., Barkume, K., Brown, M. E., et al. 2006, *ApJ*, 639, 1238, doi: [10.1086/499575](https://doi.org/10.1086/499575)
- Rabinowitz, D. L., Schaefer, B. E., & Tourtellotte, S. W. 2007, *AJ*, 133, 26, doi: [10.1086/508931](https://doi.org/10.1086/508931)
- Roberts, A. C., & Muñoz-Gutiérrez, M. A. 2021, *Icarus*, 358, 114201, doi: [10.1016/j.icarus.2020.114201](https://doi.org/10.1016/j.icarus.2020.114201)
- Rousselot, P., Korsun, P., Kulyk, I., Petit, J.-M., & Guilbert-Lepoutre, A. 2015, in *AAS/Division for Planetary Sciences Meeting Abstracts*, Vol. 47, *AAS/Division for Planetary Sciences Meeting Abstracts #47*, 211.02
- Rousselot, P., Korsun, P. P., Kulyk, I., Guilbert-Lepoutre, A., & Petit, J. M. 2016, *MNRAS*, 462, S432, doi: [10.1093/mnras/stw3054](https://doi.org/10.1093/mnras/stw3054)

- Rousselot, P., Petit, J. M., Poulet, F., & Sergeev, A. 2005, *Icarus*, 176, 478, doi: [10.1016/j.icarus.2005.03.001](https://doi.org/10.1016/j.icarus.2005.03.001)
- Santos-Sanz, P., Lellouch, E., Groussin, O., et al. 2017, *A&A*, 604, A95, doi: [10.1051/0004-6361/201630354](https://doi.org/10.1051/0004-6361/201630354)
- Sarid, G., Volk, K., Steckloff, J. K., et al. 2019, *ApJL*, 883, L25, doi: [10.3847/2041-8213/ab3fb3](https://doi.org/10.3847/2041-8213/ab3fb3)
- Scargle, J. D. 1982, *ApJ*, 263, 835, doi: [10.1086/160554](https://doi.org/10.1086/160554)
- Schaefer, B. E., Buie, M. W., & Smith, L. T. 2008, *Icarus*, 197, 590, doi: [10.1016/j.icarus.2008.05.003](https://doi.org/10.1016/j.icarus.2008.05.003)
- Schaefer, B. E., & Rabinowitz, D. L. 2002, *Icarus*, 160, 52, doi: [10.1006/icar.2002.6958](https://doi.org/10.1006/icar.2002.6958)
- Schaefer, B. E., Rabinowitz, D. L., & Tourtellotte, S. W. 2009, *AJ*, 137, 129, doi: [10.1088/0004-6256/137/1/129](https://doi.org/10.1088/0004-6256/137/1/129)
- Schaller, E. L., & Brown, M. E. 2007a, *ApJL*, 659, L61, doi: [10.1086/516709](https://doi.org/10.1086/516709)
- Schaller, E. L., & Brown, M. E. 2007b, in *AAS/Division for Planetary Sciences Meeting Abstracts*, Vol. 39, *AAS/Division for Planetary Sciences Meeting Abstracts #39*, 49.10
- Seccull, T., Fraser, W. C., Puzia, T. H., Fitzsimmons, A., & Cupani, G. 2019, *AJ*, 157, 88, doi: [10.3847/1538-3881/aafbe4](https://doi.org/10.3847/1538-3881/aafbe4)
- Sheppard, S. S. 2007, *AJ*, 134, 787, doi: [10.1086/519072](https://doi.org/10.1086/519072)
- Sheppard, S. S., & Jewitt, D. C. 2002, *AJ*, 124, 1757, doi: [10.1086/341954](https://doi.org/10.1086/341954)
- Shingles, L., Smith, K. W., Young, D. R., et al. 2021, *Transient Name Server AstroNote*, 7, 1
- Shkuratov, Y., Ovcharenko, A., Zubko, E., et al. 2002, *Icarus*, 159, 396, doi: [10.1006/icar.2002.6923](https://doi.org/10.1006/icar.2002.6923)
- Silva, A. M., & Cellone, S. A. 2001, *Planet. Space Sci.*, 49, 1325, doi: [10.1016/S0032-0633\(01\)00052-6](https://doi.org/10.1016/S0032-0633(01)00052-6)
- Smith, K. W., Smartt, S. J., Young, D. R., et al. 2020, *PASP*, 132, 085002, doi: [10.1088/1538-3873/ab936e](https://doi.org/10.1088/1538-3873/ab936e)
- Thirouin, A., Noll, K. S., Ortiz, J. L., & Morales, N. 2014, *A&A*, 569, A3, doi: [10.1051/0004-6361/201423567](https://doi.org/10.1051/0004-6361/201423567)
- Thirouin, A., Ortiz, J. L., Duffard, R., et al. 2010, *A&A*, 522, A93, doi: [10.1051/0004-6361/200912340](https://doi.org/10.1051/0004-6361/200912340)
- Tholen, D. J. 1984, PhD thesis, University of Arizona
- Tholen, D. J., & Buie, M. W. 1997, *Icarus*, 125, 245, doi: [10.1006/icar.1996.5494](https://doi.org/10.1006/icar.1996.5494)
- Tholen, D. J., & Tedesco, E. F. 1994, *Icarus*, 108, 200, doi: [10.1006/icar.1994.1054](https://doi.org/10.1006/icar.1994.1054)
- Tiscareno, M. S., & Malhotra, R. 2003, *AJ*, 126, 3122, doi: [10.1086/379554](https://doi.org/10.1086/379554)
- Tonry, J. L., Denneau, L., Heinze, A. N., et al. 2018a, *PASP*, 130, 064505, doi: [10.1088/1538-3873/aabadf](https://doi.org/10.1088/1538-3873/aabadf)
- Tonry, J. L., Denneau, L., Flewelling, H., et al. 2018b, *ApJ*, 867, 105, doi: [10.3847/1538-4357/aae386](https://doi.org/10.3847/1538-4357/aae386)
- Trujillo, C. A., Brown, M. E., Barkume, K. M., Schaller, E. L., & Rabinowitz, D. L. 2007, *ApJ*, 655, 1172, doi: [10.1086/509861](https://doi.org/10.1086/509861)
- Vaghi, S. 1973, *A&A*, 24, 41
- van der Walt, S., Colbert, S. C., & Varoquaux, G. 2011, *Computing in Science and Engineering*, 13, 22, doi: [10.1109/MCSE.2011.37](https://doi.org/10.1109/MCSE.2011.37)
- Van Rossum, G. 2020, *The Python Library Reference*, release 3.8.2 (Python Software Foundation)
- VanderPlas, J. T. 2018, *ApJS*, 236, 16, doi: [10.3847/1538-4365/aab766](https://doi.org/10.3847/1538-4365/aab766)
- Đurech, J., Kaasalainen, M., Marciniak, A., et al. 2007, *A&A*, 465, 331, doi: [10.1051/0004-6361:20066347](https://doi.org/10.1051/0004-6361:20066347)
- Verbiscer, A., & Helfenstein, P. 1998, in *Astrophysics and Space Science Library*, Vol. 227, *Solar System Ices*, ed. B. Schmitt, C. de Bergh, & M. Festou, 157, doi: [10.1007/978-94-011-5252-5_8](https://doi.org/10.1007/978-94-011-5252-5_8)
- Verbiscer, A. J., Helfenstein, P., & Buratti, B. J. 2013, in *Astrophysics and Space Science Library*, Vol. 356, *Astrophysics and Space Science Library*, ed. M. S. Gudipati & J. Castillo-Rogez, 47, doi: [10.1007/978-1-4614-3076-6_2](https://doi.org/10.1007/978-1-4614-3076-6_2)
- Verbiscer, A. J., Porter, S., Benecchi, S. D., et al. 2019, *AJ*, 158, 123, doi: [10.3847/1538-3881/ab3211](https://doi.org/10.3847/1538-3881/ab3211)
- Verbiscer, A. J., Helfenstein, P., Porter, S. B., et al. 2022, *PSJ*, 3, 95, doi: [10.3847/PSJ/ac63a6](https://doi.org/10.3847/PSJ/ac63a6)
- Virtanen, P., Gommers, R., Oliphant, T. E., et al. 2020, *Nature Methods*, 17, 261, doi: [10.1038/s41592-019-0686-2](https://doi.org/10.1038/s41592-019-0686-2)
- Volk, K., & Malhotra, R. 2008, *ApJ*, 687, 714, doi: [10.1086/591839](https://doi.org/10.1086/591839)
- Waskom, M. 2021, *The Journal of Open Source Software*, 6, 3021, doi: [10.21105/joss.03021](https://doi.org/10.21105/joss.03021)
- Wisniewski, W. Z., Michałowski, T. M., Harris, A. W., & McMillan, R. S. 1997, *Icarus*, 126, 395, doi: [10.1006/icar.1996.5665](https://doi.org/10.1006/icar.1996.5665)
- Womack, M., Sarid, G., & Wierzbos, K. 2017, *PASP*, 129, 031001, doi: [10.1088/1538-3873/129/973/031001](https://doi.org/10.1088/1538-3873/129/973/031001)